FIELD CONTROL AND OPTICAL FORCE ENHANCEMENT WITH

APERIODIC NANOSTRUCTURES

A Dissertation

Submitted to the Faculty

of

Purdue University

by

Yu-Chun Hsueh

In Partial Fulfillment of the

Requirements for the Degree

of

Doctor of Philosophy

December 2018

Purdue University

West Lafayette, Indiana

THE PURDUE UNIVERSITY GRADUATE SCHOOL
STATEMENT OF DISSERTATION APPROVAL

Dr. Kevin J. Webb, Chair
> School of Electrical and Computer Engineering

Dr. Andrew M. Weiner
> School of Electrical and Computer Engineering

Dr. Dan Jiao
> School of Electrical and Computer Engineering

Dr. Peter Bermel
> School of Electrical and Computer Engineering

Approved by:
> Dr. Pedro Irazoqui
>> Head of the School of Electrical and Computer Engineering

To My Family

ACKNOWLEDGMENTS

I would like to express my sincere appreciation and respect to my advisor, Prof. Kevin J. Webb, for his faith in me, as well as for his guidance and kindness. His insight and enthusiasm have greatly impacted me and this work. I would also like to thank my committee members, Prof. Andrew M. Weiner, Prof. Dan Jiao, and Prof. Peter Bermel for their time and advice on this work. Moreover, I thank my colleagues, Dr. Esther H. R. Tsai, Dr. Jason A. Newman, Dr. Yulu Chen, Dr. Mengren Man, Dergan Lin, John Luo, Li-Fan Yang, Justin A. Patel, Vivek Raghuram, Ryan L. Hastings, and Andrew Velzen for their assistance, contributions and friendship.

I want to thank my parents, my brother, and my wife, Alice Hu, for their love and support.

I thank God for making all things possible. "Trust in the Lord with all your heart and lean not on your own understanding; in all your ways submit to him, and he will make your paths straight."

TABLE OF CONTENTS

LIST OF TABLES

LIST OF FIGURES

Figure   Page

ABSTRACT

Yu-Chun Hsueh PhD, Purdue University, December 2018. Field Control and Optical Force Enhancement with Aperiodic Nanostructures.   Major Professor: Kevin J. Webb.

Aperiodic structures offer new functionalities for control, manipulation, and sensing that can benefit applications in all frequency ranges. We present a study of the influence of the degrees of freedom from a binary aperiodic nanostructure in free space, where each pixel is either the scatterer or the background, that uses a multivariate statistical analysis to examine the covariance matrix of the output field distributions. The total variance of the output fields and the rank can be evaluated to provide quantitative measurements of control. In addition, the field statistics provide an improved understanding of the scattering properties of aperiodic structures.

It has been proposed that structuring a metal surface can substantially increase the optical pressure over that possible with a planar interface. Based upon the forces on the mirrors of a one-dimensional asymmetric Fabry-Perot cavity, we show that the sum of the pressures on both mirrors increases through asymmetry and with quality factor. Using cavity quality factor as a measure, we present the physical basis of the enhanced pressure on a nanostructured metallic surface as being due to an array of asymmetric resonant cavities.

With use of optimized, aperiodic structures, more control and higher pressure should be possible. We present a design method by which the electromagnetic pressure on a nanostructured binary material can be controlled in terms of both the enhancement and the direction. This analysis offers new avenues for optomechanics.

1. INTRODUCTION

Aperiodic nanostructures offer new functionalities to control the spatial and temporal field on the nanoscale. Recent work on transmission matrices connects specific eigenmodes from the output field to the input field, and gives a fundamental view for the study of random media [1]. By using multiresolution optimization, compact and high performance mode converters, filters, and special reflectors can be achieved in various spectral ranges, facilitated by the large number of degrees of freedom provided by engineered aperiodic structures [2–5]. Missing has been the understanding of the possible degrees of control and efficient methods to support design strategies. A bound for control over propagating scattered fields has been investigated in relation to the properties of the structure [6]. In addition, the increase in degrees of freedom from multidimensional aperiodic volume optics has been demonstrated, allowing the structures to achieve multiplex functions [7]. However, in the previous work, only propagating modes are considered to find the limit of control. The potential of near-field control, where evanescent fields contribute, remains unexplored. Furthermore, because the first Born approximation is no longer applicable under strong scatter. the relationship between scatterer variables and the scattered fields is a nonlinear problem which relies on numerical solutions. In Chap. 2, we apply multivariate statistical analysis and extract information from the field covariance matrix to analyze the dependence of degrees of freedom available from binary aperiodic structures. The field statistics, corresponding to newly introduced circular Bessel statistics [8,9], are also studied.

Cavity dynamics concepts for the radiation pressure on a mirror are based on the classical picture from Maxwell in the appropriate limit, where $P = S(1+|\Gamma|^2)/v$, with Γ the field reflection coefficient, v the background medium velocity, and S the magnitude of the incident Poynting vector. Clearly, increasing intensity or the incident

Poynting vector by increasing the cavity quality factor (Q) will increase the pressure on the mirror. For example, the attractive or repulsive forces between coupled dielectric cavities have been found to be enhanced by the cavity Q [10]. This background would suggest that the maximum radiation pressure on a mirror is $2S/v$. However, based on a structured metal surface with cavities that support a metal-insulator-metal (MIM) waveguide mode resonance, it has been proposed that the pressure, defined as the force density integrated over a periodic material and divided by the unit cell area, can be substantially larger [11]. This enhanced pressure phenomenon was shown to be resonance-based, whereby adjusting the dimensions on the small cavities formed in a metal surface varies the pressure from essentially $2S/v$ to a value more than an order of magnitude higher. In Chap. 3, we present a physical explanation that is based on an asymmetric Fabry-Perot cavity and the cavity Q, and relate this to the situation with a metal surface having an array of MIM-mode cavities.

Optical force is related to a change in momentum and also field spatial distribution. Progress on describing the optical force within homogeneous bulk materials [12], small objects [13] and periodic structures [14] has revealed some important understanding about optical manipulation. Nevertheless, aperiodic structures can provide a large number of degrees of freedom and hence more electromagnetic field control relative to periodic systems. Previous results show that some unintuitive realizations for waveguide [2–4, 15–17] and diffractive [5] elements can be achieved from aperiodic-structured material to present functions that are not possible with conventional concepts, such as those involved periodic structures. Based on our experiences and understanding on aperiodic nanostructured materials in Chap. 2, we are particularly interested in how the large degrees of freedom supported by aperiodic materials may contribute on the control of the optical force. In Chap. 4, we show that, with use of dielectric/metallic scattering materials, the optical pressure can be controlled in terms of both the enhancement level and direction, and that this can be understood from the field variance with binary aperiodic nanostructures.

In Chap. 5, we provide conclusions, including the potential impact of this work. Several opportunities as extensions of this work are summarized.

2. FIELD CONTROL WITH BINARY APERIODIC NANOSTRUCTURES[†]

Aperiodic, irregular structures offer a large number of degrees of freedom relative to periodic or quasi-periodic systems and hence the opportunity for more control over electromagnetic fields. The challenge is to understand the relation between structure and material and the possible response, as measured by achievable scattered field as a function of position and frequency. With this information, basic guidelines could become available to facilitate a computational design process. Having this goal in mind, near-field through far-field control is appraised through a multivariate statistical analysis of example binary two-dimensional nanostructured aperiodic material arrangements. The total variance and significant rank of the transmission matrix, equivalent to the field correlation at the detector plane in the situations treated, yields quantitative measures of the degree of control related to size, material properties, and material spatial decomposition. This analysis provides design guidelines for aperiodic structures that can control light as a function of position and frequency in new ways.

2.1 Introduction

The control of light through the use of structured materials such as dielectric stacks, photonic crystals, metamaterials, and random nanostructures presents opportunities to expand the design space for devices that require the manipulation of the spatial, spectral and temporal character of electromagnetic fields. Photonic crystals have been widely studied, and proposed as a means to control the spontaneous emis-

---

[†]This work is published as Yu-Chun Hsueh and Kevin J. Webb, "Electromagnetic field control with binary aperiodic nanostructures," *J. Opt. Soc. Am. B*, 34, 2059-2071, 2017 (Ref. [18])

sion of materials [19] and affect localization [20]. These engineered periodic structures can support light confinement within a wavelength-sized volume without substantial loss, enhancing light-matter interaction. A quasi-crystal, which is a structure class having particular order but is not periodic in the sense of replication of a primitive unit cell, was discovered to present unique and rich symmetries in Fourier space that are not possible with a periodic structure [21]. Such quasi-crystalline structures provide more degrees of freedom than periodic systems. Even more degrees of freedom are possible with irregular, aperiodic elements, where in a design scenario some region of a material space could be decomposed using a basis set and a cost function optimized over the free variables to design a structure. However, unlike photonic crystals, where there is a well-established theoretical foundation from the work of Bragg, Brillouin, Floquet, Bloch and others, few guidelines exist for aperiodic scattering elements, and rather unintuitive designs for waveguide [2–4, 15–17] and diffractive [5, 7] elements have resulted from optimization-based solutions.

Progress on basic understanding has been made by counting the propagating modes, resulting in bounds that can be related to a weakly scattering medium description [6, 22–25]. A far-field bound for controlling propagating modes has been considered, with the equivalent sources (scatterers) and the fields in particular spaces [6, 24]. Of relevance here, it has been proposed that the maximum number of orthogonal modes (M) that can be generated in a space is bounded by $M \leq \sqrt{N_C N_{GS}}$, where N_C is a bound prescribed by the properties of the material and structure, and N_{GS} is determined by the free space Green's function. This work was extended to find a bound for two-dimensional passive devices for multiple scattering modes [25]. A full cylinder that contains all scatterers and a receiving outer ring in the far-field were considered in order to find another bound on the total number of scattering modes. Because the number of strongly scattered modes cannot exceed the total number of modes, a bound results that increases with permittivity until it saturates. Summarizing, with propagating modes, each addressable volume becomes about half

a wavelength on a side, and the variables within the scattering structure dictate possible control over this mode set, i.e., the fields in each addressable volume.

The relationship between the structure (material properties as a function of space) and the field is nonlinear, but becomes linear with weak scatter and validity of the first Born approximation. With linearity comes a particularly simple picture relating the structure to the field control space. Our interest here encompasses the near-field, where the evanescent fields allow the addressable volume to approach zero, and in material decomposition as a function of position, with varying and potentially strong scatter. This provides a more general framework for irregular structures in waveguide and diffractive element configurations that will guide the design of aperiodic volume optical elements [7].

The propagation of optical waves in multiple scattering media is a fundamental physical problem. Knowledge of the transmission matrix, part of the scattering matrix, gives a fundamental description for the study of complex media [26]. The transmission matrix for a given wavelength generally consists of a set of complex coefficients connecting a set of modes describing the output field to those of the input field. Transmission matrix information therefore describes the polarization-dependent control of a structure. The monochromatic transmission matrix for a random medium has been obtained with spatial light modulator control of the incident light and a full-field interferometric measurement [1]. Such transmission matrix information has allowed focusing and imaging through random media [1, 27–33]. In dissipative random media, the density of transmission and reflection eigenvalues has been shown to depend on the strength of absorption [34–37] as well as the geometry of the system [38]. The increase in the degrees of freedom from volumetric devices allows structures to multiplex functions, expanding the traditional capabilities in various applications [22, 23, 25].

Here, we consider the near-field, where the evanescent field spectrum is important, through to the far-field, where only the propagating part of the plane wave spectrum contributes, and use a statistical measure to understand the influence of various as-

pects of the scattering element control, as will be useful in the design process. The most important measure becomes the variance of the field correlation matrix in the detection region. We note that intensity variance has been used, for example, in randomly scattering media to determine the onset of localization [39–41], and that strong scatter can be important in field control with aperiodic elements. Consequently, we provide a foundation for waveguide and diffractive element devices that can have functionality and performance beyond that possible with more constrained spatial variations on material and structure.

The 2D scattering problem of Fig. 2.1 is considered with TM polarization (the magnetic field is transverse to the axis of the cylinder) having fields E_z, H_x, H_y, where the coordinate system of Fig. 2.1 is used and E_i and H_j are the scalar components of the electric and magnetic fields, respectively. We analyze the dependence of the degrees of freedom available for controlling the output field, along a line shown on the right of Fig. 2.1 some distance d from the back surface of the scattering control element, using a multivariate statistical analysis. We investigate the scattered field statistics. We also discuss the connection between the field correlation matrix studied here and the transmission matrix. The relationship between the structure and the field control metrics provided leads to an understanding that can be exploited in applications.

We describe the relationship between the aperiodic scattering element and the fields in Section 2.2. This sets the stage for the statistical development based on the transmission matrix and, in our situation, the detector field correlation matrix, presented in Section 2.3. Section 2.4 presents statistical results for binary aperiodic scattering elements that provides a basis for understanding the structure-field relationship. Section 2.5 describes the field statistics for aperiodic elements, and indicates that there is a regime with strong scatter where newly introduced circular Bessel statistics that have been shown to describe Anderson localization fit nicely. We draw some conclusions that guide future work in Section 2.6.
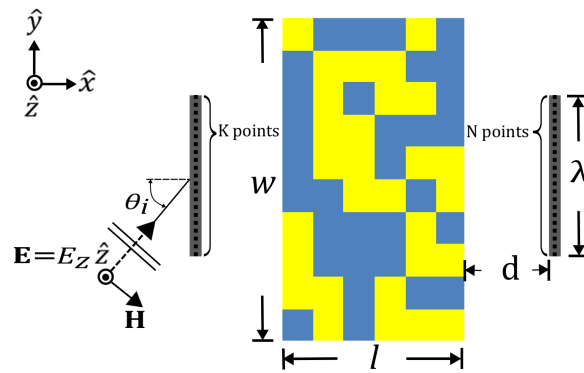
Fig. 2.1. Binary aperiodic nanostructured material with width w and length l. A TM plane wave (E_z is out of plane) is incident from the left at angle θ_i to normal and a detector line of length λ is placed at a distance of d away from the structure on the right. The incident and detector line are uniformly divided giving K and N positions, respectively.

2.2 Structure-Field Relationship

We introduce the structure-field relationship through the integral equation representation of scatter from inhomogeneities. The inhomogeneous TM source-free scalar wave equation is

$$\nabla \cdot \frac{1}{\mu}\nabla\phi + k_0^2\epsilon\phi = 0, \tag{2.1}$$

where $\phi = E_z$ in our case, μ and ϵ are the relative permeability and the dielectric constant, respectively, and k_0 is the free space wave number. A solution for E_z from (2.1) yields the magnetic field through Faraday's law and hence the complete field solution for a 2-D problem. Consider $\epsilon = \epsilon_b + \Delta\epsilon$ for the nonmagnetic case ($\mu = 1$), where ϵ_b describes the background dielectric constant and $\Delta\epsilon$ the change, creating the inhomogeneous material. Equation (2.1) then becomes

$$\nabla^2\phi + k_0^2\epsilon_b\phi = -k_0^2\Delta\epsilon\phi. \tag{2.2}$$

Using the Green's function for (2.2), the integral equation becomes

$$\begin{aligned}
\phi(\mathbf{r}) &= \phi_i(\mathbf{r}) + \phi_s(\mathbf{r}) \\
&= \phi_i(\mathbf{r}) + \int dv' k_0^2\Delta\epsilon(\mathbf{r}')\phi(\mathbf{r}')G(\mathbf{r},\mathbf{r}'),
\end{aligned} \tag{2.3}$$

where ϕ is the total field, ϕ_i is the incident field (that without the scatterer), and ϕ_s is the scattered field, given as a superposition integral within v' with the Green's function $G(\mathbf{r},\mathbf{r}')$, and with $\mathbf{r}'$ the source point vector. When $\phi \approx \phi_i$ in the integrand of (2.3), a linear solution of (2.3) is given by the first Born approximation [42]. However, when the scattering becomes strong, additional terms in a series expansion are necessary, or a more general treatment of the nonlinear problem is needed. Our interest here is the influence of the degrees of freedom for multidimensional devices with potentially strongly scattered fields, especially in the near-field region. Measures of the nonlinear relationship between scattered fields and the scatterer variables thus becomes key to develop insight.

We take the approach of measuring the field in the control volume using randomly chosen components of the scattering element and with a specific incident field. In this way, we can evaluate statistical information. This amounts to determining the field correlation along a detector line. We then investigate the eigenvalue problem associated with the field correlation matrix, thereby learning of the control of the field.

2.3 Mathematical Description of Aperiodic Elements

We consider a 2-D geometry for computational expediency, with the understanding that essential information such as evanescent fields that apply to 3-D can be captured. Figure 2.1 shows a 2-D aperiodic nanostructure in free space with binary scattering elements, where each pixel can be one of two materials, the scattering material or the background. To analyze the dependence of the degrees of freedom available for controlling the output field, the nanostructure is divided as a $M = P \times Q$ uniform array, with each pixel either the scattering material m_1 (with dielectric constant ϵ_1) or the background m_2 (with dielectric constant ϵ_2). Material m_1 has a fill factor f and the background material, m_2, has fill $1 - f$. The scatterer spatial support has width w and length l, both comparable to the wavelength in the background medium.

An incident TM plane wave (E_z is out of page in Fig. 2.1) is incident from the left throughout this work, and the incident field for computational purposes is assumed to be the $x =$ constant line at the left boundary of the structure. The detector line is placed at a variable distance d from the right surface of the scatter. We use a numerical method to find the scattered field (E_z), as described in Sect. 2.4, and all other quantities are found as secondary parameters, including the magnetic field ($\mathbf{H}$) and the metrics for evaluating field control that we present here.

We discuss the connection between the transmission matrix, used for describing random media [1, 26], and our field analysis that allows evaluation of control with binary aperiodic elements. The (K, N) transmission matrix $\mathbf{T}$ can be defined as

$$\mathbf{T} = \left[\frac{E_n}{E_{i,k}} \right], \quad k \in [1, ..., K] \quad n \in [1, ..., N], \tag{2.4}$$

where $E_{i,k}$ is the incident field at points along the input line, E_n is the total field along points on the output line, and the subscripts n and k indicate positions on the detector line and the input line, respectively, for the 2-D situation depicted in Fig. 2.1. In this case, the detector line and the input line are divided into N and K points, respectively. We define the field covariance matrix, $\mathbf{C}$, as

$$\mathbf{C} = \langle \mathbf{T}^H \mathbf{T} \rangle - \langle \mathbf{T}^H \rangle \langle \mathbf{T} \rangle, \tag{2.5}$$

where the averaging is over all observations, and the entries correspond to the various positions on the detector line. One observation means the output electric field at a point on the detector line for a particular nanostructured scattering material arrangement, given an incident field at some point on the input line. Each arrangement here follows the rule we defined with a fill factor f for the scattering material m_1. We consider incident plane waves, initially with normal incidence and then with oblique incidence. The field at the various points along the input line therefore have a simple relationship - they are equal or have equal magnitude and uniform phase progression.

A large variance at a particular position indicates that the binary arrangement has a large impact on adjusting the output electric field, thus suggesting more efficacy or increased degrees of freedom for field control. We apply a principal component analysis [43, 44] to decompose the field covariance and extract information for comparisons of the influence of various degrees of freedom in the scattering elements. The covariance matrix ($\mathbf{C}$) is Hermitian and positive semi-definite, such that all eigenvalues (λ_i) are non-negative [45], where i indicates that the eigenvalue is from the i-th principal component. The λ_i describe the strength of the variance along the corresponding principal components. Therefore, the average total variance, σ_C^2, that the aperiodic

nanostructure provides along the detector line can be determined by the sum of the eigenvalues of $\mathbf{C}$ as

$$\sigma_C^2 = \sum_{i=1}^{N} \lambda_i = \text{Tr}\{\mathbf{C}\}, \tag{2.6}$$

where Tr indicates the trace of the matrix, the sum of the diagonal elements. The first equality in (4.7) results because the deviation of $\mathbf{C}$ is measured in the definition of (4.4) and the second can be proved from the characteristic polynomial of the eigenvalue problem [45]. We may further define a normalized cross-correlation matrix $\mathbf{R}$ by

$$
\begin{aligned}
\mathbf{R} &= \begin{bmatrix} R_{rs} \end{bmatrix} \\
&= \begin{bmatrix} \dfrac{C_{rs}}{\sqrt{C_{rr}}\sqrt{C_{ss}}} \end{bmatrix},
\end{aligned} \tag{2.7}
$$

where C_{rs} is the element of the covariance matrix $\mathbf{C}$, and $r,\ s\ =\ 1, 2, ..., N$. $\mathbf{R}$ is thus normalized so that each element satisfies $0 \leqslant \left| R_{rs} \right| \leqslant 1$, with the upper bound attainable only when the two data are completely correlated. Therefore, the total variance from the field normalized correlation matrix, $\mathbf{R}$, is:

$$
\begin{aligned}
\sigma_R^2 &= \text{Tr}\{\mathbf{R}\} \\
&= \sum_{n=1}^{N} \frac{C_{nn}}{\sqrt{C_{nn}}\sqrt{C_{nn}}} \\
&= N.
\end{aligned} \tag{2.8}
$$

From (2.8), the total variance σ_R^2 is always equal to the number of variables, N, no matter how the other parameters vary. Thus, the information to compare different data tables has been eliminated after self-normalization, making (2.8) unsuitable. This position will be supported by an example from our simulations that compares the unnormalized ($\mathbf{C}$) and normalized ($\mathbf{R}$) pictures. Summarizing, a covariance principal component analysis based on (4.4) and (4.7) will be applied to appraise aperiodic element control.

The number of the significant components indicates how many channels an aperiodic structure provides for controlling the output field. Because the importance of

a component is reflected in the proportion of its corresponding eigenvalue (variance) to the total variance, we define the rank as the number of the components which contains over the percentage we specify of the total variance.

The electric energy density associated with the incident field is $w_{ei} = \epsilon_0\epsilon_2|E_i|^2/2$, where ϵ_0 is the free space permittivity. Therefore, the average output electric energy density is $\langle w_{e,n}\rangle = \langle\epsilon_0\epsilon_2|E_n|^2/2\rangle$, where the averaging is over observations at point n on the detector line with differing scattering elements. We define the normalized transmitted average electric energy as

$$W_{ea} = \frac{\sum_{n=1}^{N}\langle w_{e,n}\rangle}{\sum_{k=1}^{K}w_{ei,k}}, \qquad (2.9)$$

where the sum is over all observed points on the detector line and $\sum_{k=1}^{K}w_{ei,k} = Kw_{ei,k}$ for our case of an incident plane wave.

We write the incident time-averaged Poynting vector as $\mathbf{S}_i = \Re\{\mathbf{E}_i \times \mathbf{H}_i^*\}/2$, where $\mathbf{E}_i$ and $\mathbf{H}_i$ are the incident electric and magnetic fields, respectively. The configurational-averaged output time-averaged Poynting vector is written as $\langle\mathbf{S}_n\rangle = \langle\Re\{\mathbf{E}_n \times \mathbf{H}_n^*\}\rangle/2$, where the averaging is over all observations at point n on the detector line. We then write the normalized average transmitted power as

$$P_{av} = \frac{\sum_{n=1}^{N}\langle\mathbf{S}_n\rangle \cdot \hat{\mathbf{n}}}{\sum_{k=1}^{K}\mathbf{S}_{i,k} \cdot \hat{\mathbf{n}}}, \qquad (2.10)$$

where the sum is over all observed points on the detector line and $\hat{\mathbf{n}}$ is the unit vector normal to the detector line.

If we assume an incident uniform plane wave, the incident electric field magnitude $|E_{in}|$ at each position on the input line is identical. We can thus write

$$\langle\mathbf{T}^H\mathbf{T}\rangle = \frac{K}{|E_i|^2}\begin{bmatrix} \langle E_1^*E_1\rangle & \langle E_1^*E_2\rangle & \cdots & \langle E_1^*E_N\rangle \\ \langle E_2^*E_1\rangle & \langle E_2^*E_2\rangle & \cdots & \langle E_2^*E_N\rangle \\ \vdots & \vdots & \ddots & \vdots \\ \langle E_N^*E_1\rangle & \langle E_N^*E_2\rangle & \cdots & \langle E_N^*E_N\rangle \end{bmatrix}, \qquad (2.11)$$

where K is the number of input variables (positions on the input line). Using the same definition as (4.7) to calculate the sum of the eigenvalues of $\langle \mathbf{T}^H \mathbf{T} \rangle$, Σ, we have

$$
\begin{aligned}
\Sigma &= \mathrm{Tr}\{\langle \mathbf{T}^H \mathbf{T} \rangle\} \\
&= \frac{K}{|E_i|^2} \sum_{n=1}^{N} \langle |E_n|^2 \rangle.
\end{aligned} \tag{2.12}
$$

Hence, (2.12) is proportional to the electric energy received by the line of detectors. A difference in magnitude with a constant K^2 can be observed between W_{ea} in (2.9) and Σ in (2.12), whereby

$$
\Sigma = K^2 W_{ea} = K \frac{\sum_{n=1}^{N} \langle w_{e,n} \rangle}{w_{ei,k}}. \tag{2.13}
$$

The binary structure with M pixels has 2^M permutations. With V observations and $V < 2^M$, where an observation in our case amounts to numerical computation of the total field at a set of points on the detector line, we need to evaluate a measure of control that is exhibited in $\mathbf{C}$ and σ_C^2. To estimate the density function for the mean, hence both the estimate and the error bars representing the standard deviation, we apply a resampling method, thereby estimating the precision of the sample statistics [46]. The detailed procedure we use is as follows. Each data table with V observations in N variables (the points along the detector line) is described as a (V, N) matrix. We randomly draw an observation vector from the original V observations with replacement. This selection is repeated V times to form a new (V, N) data table. We then apply principal component analysis to this new table to obtain the statistics as an estimate from the population. Averaging over the V observations allows $\mathbf{C}_v$ for $v = 1, ..., V$ to be determined, yielding an estimate of the mean and the error in estimating the mean. In prior work, it was found that about 50 samples were needed to reduce the simulation error to an acceptable level [46, 47]. In our simulations, we repeat this procedure 100 times to obtain adequate sampling, yielding the means and error bars in the data we present.

Finally, consider a simple illustration. A plane wave propagating in free space that is normally incident on the detector line has constant output electric field. The

covariance matrix, $\mathbf{C}$, from (4.4), is a null matrix, where the corresponding eigenvalues and rank are all zero. Therefore, the variance is zero without the presence of scatterers. Next, if a plane wave passes through an aperiodic arrangement of weak scatterers, there will be relatively small fluctuations of the field along the detector line. Because the total variance with weak scatter remains small, there is little field control. This leads to the need to understand the relation between relatively strongly scattering aperiodic media and control over fields at a set of detector points. We pursue this understanding based on example numerical simulation studies.

2.4   Numerical Results for Field Control with Aperiodic Elements

Section 2.4.1 presents numerical results for control with dielectric aperiodic structures and normally incident light. Section 2.4.2 explores the situation with oblique incidence, and Sect. 2.4.3 considers the merits of lossless metallic scatters (having a negative real dielectric constant) as aperiodic control elements. The eigenvalues of $\mathbf{C}$ in (4.4) are calculated to obtain the largest eigenvalue, λ_1, and the total variance, σ_C^2, is thus found from (4.7). The Matlab function *eig* was used to compute the eigenvalues [48], which involves use of the the QZ algorithm, also known as the generalized Schur decomposition, to determine the eigenvalues and eigenvectors. This function was tested with several examples, and we confirmed that the sum of eigenvalues from the *eig* function is equal to the trace of the matrix. The rank is defined here by the number of eigenvalues of $\mathbf{C}$ that represent some fraction of the total variance, σ_C^2, and we show results for three thresholds: 1%, 10^{-5}%, 10^{-10}% of σ_C^2. The normalized transmitted average electric energy, W_{ea}, is plotted according to (2.9). The normalized average transmitted power, P_{av}, is obtained from (2.10). The sum of the eigenvalues for $\langle \mathbf{T}^H \mathbf{T} \rangle$, Σ, is determined from (2.12).

The structure variables are shown in Fig. 2.1, and throughout, the background is assumed to be free space. All results are generated from a 2-D numerical (finite element method, FEM) solution (using COMSOL [49]) with sufficient accuracy to

establish these parameters as metrics for evaluating control prospects with aperiodic elements. The numerical formulation is chosen to solve for the scattered field, and the total field used in the numerical analysis is obtained by adding the incident field. In our computational domain, the scattering structure is located at the center of background region having size $10\lambda \times 10\lambda$, which in turn is enclosed by perfectly matched layers to simulate unbounded space. Unless indicated otherwise, the background wavelength used in the calculations is $\lambda = 700$ nm. Based on scaling in Maxwell's equations, neglecting dispersion, the results apply at any wavelength. In some cases, the wavelength is used as a parameter. Throughout, the numerical field calculations assume the incident plane wave has a power density of 1 W/m^2.

The total electric field (incident plus scattered), E_z, on the detector line d behind the scatterer (see Fig 2.1) is calculated for each particular arrangement of the structure. The detector line of length λ is uniformly divided into 100 segments, giving $N = 101$ detector positions (the variable positions for the data table). This procedure is repeated 300 times for random instances of the binary structure to obtain a suitable amount of data for averaging. We use these observations to calculate the 101×101 covariance matrix, $\mathbf{C}$, and its eigenvalue decomposition, to observe control as measured by the variance in (4.7). The mean values and the error bars at each data point are calculated from the mean and the standard deviation of the resampling distribution, where the number of samples is 100 in our simulations.

2.4.1   Normal Incidence - Dielectric Elements

For normal incidence, the plane wave is incident in the x-direction in Fig. 2.1. We initially consider a structure of dimension $\lambda \times \lambda$ (see Fig. 2.1), and background $\lambda = 700$ nm. Because weak scatter cannot support a large variance for control of the output field, we focus on the strong scattering cases. We consider silicon, $\epsilon_1 = 12.38$ [50], placed in free space with $\epsilon_2 = 1$, such that $\Delta\epsilon = \epsilon_1 - \epsilon_2 = 11.38$. The scatterer resolution $\{P, Q\}$, the uniform discretization (pixellation) of the $\lambda \times \lambda$

domain, is first chosen to be $\{3, 3\}$, with a fixed filling factor f specified by enforcing 4 of the total of 9 elements to be scatterers and the remaining 5 elements to be the background material, free space.

Figure 2.2(a) gives σ_C^2 as a function of d, where the symbols are the calculated data points. The larger σ_C^2 for small d, close to the structure, indicates the additional control with evanescent fields. As d recedes to the far field, the fixed detector length of λ results in diminishing control. To explain this, consider that in the far-field region a wave from a compact radiator behaves as a spherical wave that at any point can be treated as a local plane wave whose electric field intensity is the same as that of the wave and whose propagation is along the radial direction from the radiator. As we indicated, a plane wave has zero degrees of freedom for controlling the output field. Figure 2.2(b) shows that the largest eigenvalue, λ_1, also decreases with increasing d, leading to a loss of control from the first principal component in the far-field region. Figure 2.2(c) shows the rank as a function of d, with varying threshold. In all cases, the rank decreases with increase in d, indicating a reduction in controllable eigenchannels with distance. Our simulations support the expected situation that the degrees of freedom decrease as the detector recedes from the detector to the far-field region. Although this effect may be exacerbated by the detector line length being fixed at λ, in general, this should hold because of loss of evanescent field information. To compare the degrees of freedom between different sets of parameters (distance in Fig. 2.2 for example), we should apply a covariance principal component analysis from (4.4) instead of a normalized analysis from (2.7). Figure 2.2(d) shows the largest eigenvalues from the normalized correlation, $\mathbf{R}$, in (2.7). The increase in λ_1 with increasing d only reflects the fact that the first principal component contains an increasing contribution relative to the other components within the same correlation matrix. Equation (2.7) is unsuitable for observing the degrees of control in our analysis, which requires absolute information. The average energy on the detector line, W_{ea}, defined by (2.9), is plotted in Fig. 2.2(e), and the average power delivered to the detector, P_{av}, defined by (2.10), in Fig. 2.2(f), both as a function of distance to the

detector line, d. Notice that although there are only slight variations in both as d is varied, σ_C^2 reduces with increasing d and fixed detector length because of the decreasing plane wave spectrum contribution. The error bars in Fig. 2.2 were determined using the resampling method, as we describe above.

A large number of degrees of freedom can be achieved in the near-field, and we consider the impact of various parameters on output field control. In Fig. 2.3(a), we plot σ_C^2 in the near-field region ($d = \lambda/8$) as a function of filling factor f, for $\{P, Q\} = \{3, 3\}$ and $\Delta\epsilon = 11.38$. The number of scattering and background segments must be integers in the binary aperiodic structure, so we round down the number of scatterers for a particular f to achieve this. For example, when f is 0.5, we have 4 of the total 9 elements as scatterers and the remaining 5 elements as background material (free space here). When f is 0 or 0.1, no scatters exist in the model, resulting in zero variance at the output. The total variance increases with increasing f in Fig. 2.3(a) because more scatterers act as controllable pixels in the nanostructure. For $f > 0.5$, the contribution to σ_C^2 by adding more scatterers saturates. The differences in degrees of freedom for f between 0.5 to 0.9 are not significant. Moreover, with $f = 1$, where the medium is homogeneous, there is no control. This suggests reduced control with fill fractions approaching unity. Figures 2.3(b) and (c) show the largest eigenvalue (λ_1) and the rank as a function of fill factor, respectively. When $f = 1$, both the largest eigenvalue and rank agree with the result from σ_C^2, supporting no control at the output. When $f = 0.9$, from Fig. 2.3(b), the first principal component provides larger variance than in the other cases, but this also results in fewer controllable eigenchannels, as shown in Fig. 2.3(c). These results suggest that when designing a binary aperiodic structure, $0.5 < f < 1$ is recommended. To observe how the volume or dimensions of the nanostructure contribute to the variance of the output fields, we simulated the nanostructures with $l = \lambda$ but different widths from $w = \lambda$ to 3λ, for $\{P, Q\} = \{3, 3\}$, $\Delta\epsilon = 11.38$ and $f = 0.5$. As shown in Fig. 2.3(d), even if f is fixed, σ_C^2 increases with structure width and hence with more controllable volume.
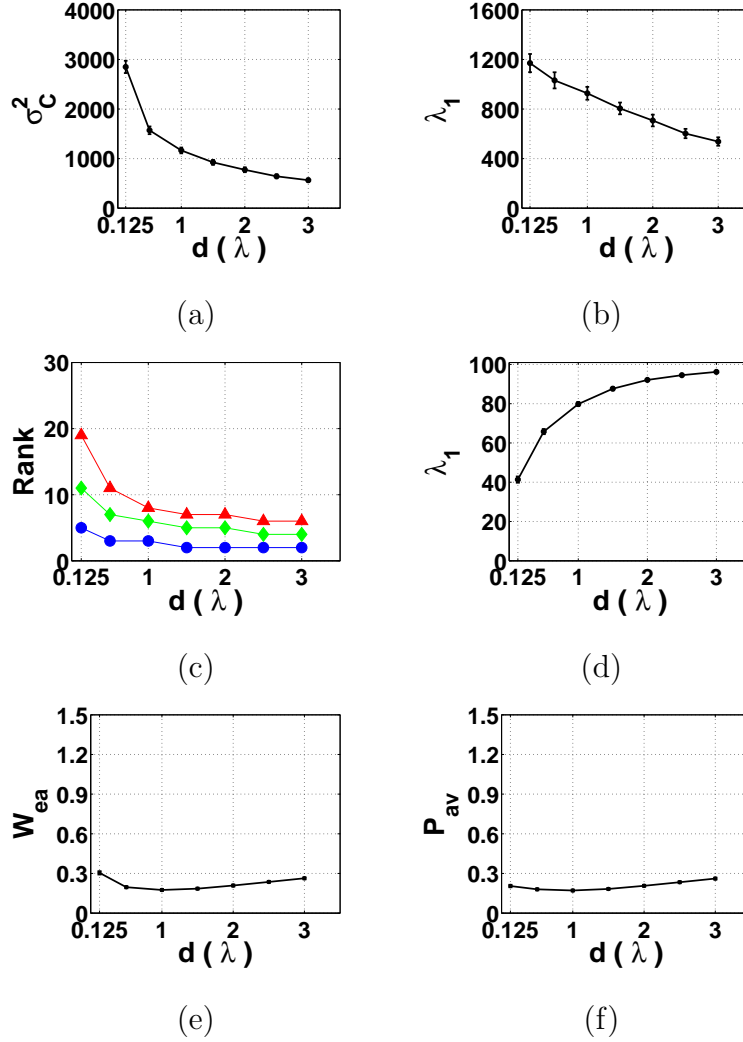
Fig. 2.2. Statistical analysis for normal incidence, $\{P, Q\} = \{3, 3\}$, $\Delta\epsilon = 11.38$, $f = 0.5$: (a) total variance, σ_C^2, plotted as a function of distance to the detector line, d (see Fig. 2.1); (b) the largest eigenvalue of $\mathbf{C}$, λ_1; (c) the rank as the number of the components which contain over 1% (blue circle), $10^{-5}\%$ (green diamond), $10^{-10}\%$ (red triangle) of σ_C^2; and (d) λ_1 from the normalized correlation, $\mathbf{R}$. (e) Normalized transmitted electric energy, W_{ea}, as a function of d; and (f) normalized transmitted power, P_{av}, as a function of d. The error bars in (a), (b), (d), (e), and (f) and as included for all other numerical results were calculated from the standard deviation of the resampling distribution where the number of samples is 100.
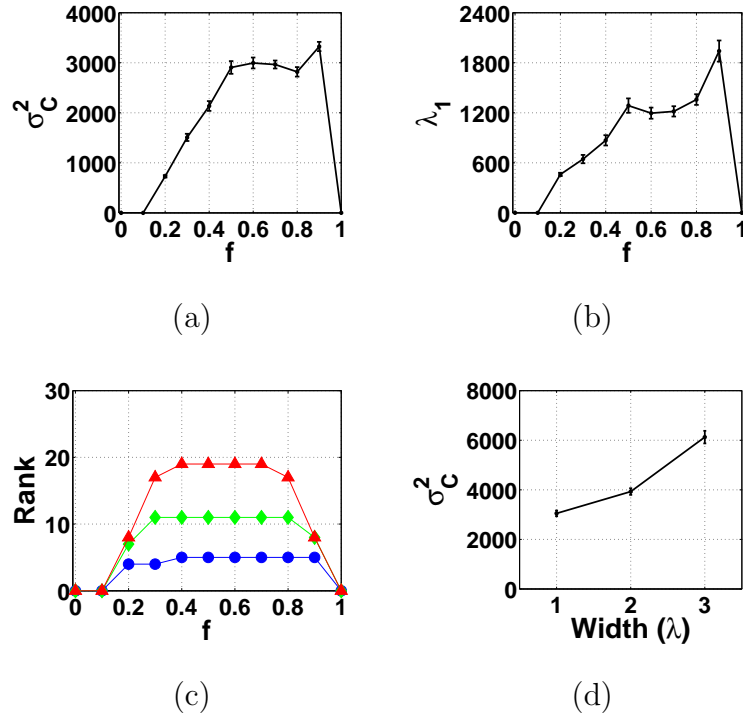
Fig. 2.3. Normal incidence, $\{P,Q\} = \{3,3\}$, $\Delta\epsilon = 11.38$, and $d = \lambda/8$: (a) σ_C^2 as a function of filling factor, f; (b) λ_1 from (a); (c) rank with varying threshold - 1% (blue circle), 10^{-5}% (green diamond), 10^{-10}% (red triangle) of σ_C^2; and (d) σ_C^2 plotted as a function of the structure width, w, with $l = \lambda$. The calculated data points with error bars are shown in (a), (b) and (d).

To investigate the influence of material property, we consider control as a function of dielectric constant in Fig. 2.4. In Fig. 2.4(a), the average energy on the detector line, W_{ea}, defined by (2.9), oscillates with increasing $\Delta\epsilon$, with more significant resonances at specific $\Delta\epsilon$. Notice that the oscillations in W_{ea} are large relative to the error bars that are also plotted. The average power delivered to the detector, P_{av} and defined by (2.10), is plotted in Fig. 2.4(b) as a function of $\Delta\epsilon$. The differences between Fig. 2.4(a) and (b) are due to the influence of evanescent fields on the energy in the near-field and the contributions of the multiple propagating plane waves along the detector line. We use the same simulation data to observe the connection between Σ from $< \mathbf{T^H T} >$ in (2.12), plotted in Fig. 2.4(c), and W_{ea} in (2.9). In (2.12), Σ is equal to $\text{Tr} < \mathbf{T^H T} >$, such that a difference in magnitude with a constant K^2 can be observed from the result of Fig. 2.4(a). K is chosen to be 101 in our simulation, and as we predict, Fig. 2.4(c) only differs from Fig. 2.4(a) by a factor of $10201 (= 101 \times 101)$.

In Fig 2.5(a), we plot σ_C^2 as a function of $\Delta\epsilon = \epsilon_1 - \epsilon_2$ for $\{P, Q\} = \{3, 3\}$ and $f = 0.5$, with all other parameters the same as the previous simulations. As expected, for $\Delta\epsilon = 0.075$, the weak scatter provides small variance. However, somewhat surprisingly, σ_C^2 oscillates with varying $\Delta\epsilon$ and the maximum occurs with $\Delta\epsilon = 3$. One reason for this apparent saturation in σ_C^2 is that the transmitted electric energy, W_{ea}, and power, P_{av}, while oscillatory, generally reduce with increasing scattering strength, as shown in Figs. 2.4(a) and (b). Stronger scattering elements in the configuration of Fig. 2.1 on average reduce the transmission, resulting in a loss of effective control and a decrease in σ_C^2. Figure 2.5(b) shows that λ_1 is similar to σ_C^2 in Fig. 2.5(a). In Fig. 2.5(c), the rank of $\mathbf{C}$ increases dramatically when $\Delta\epsilon$ increases from 0.075 to 3, but then varies only slightly with increasing $\Delta\epsilon$. It appears that for the physical situation we consider, larger $\Delta\epsilon$ does not guarantee more degrees of freedom, and that one should select a material with a proper dielectric constant to be resonant within a limited range in an application. From the best case ($\Delta\epsilon = 3$) in our simulations, a material with dielectric constant around 3 to 9 in the visible range appears effective and is available. Figures 2.5(a)-(c) are for $f = 0.5$, which means we lose some combi-

(a)

(b)

(c)
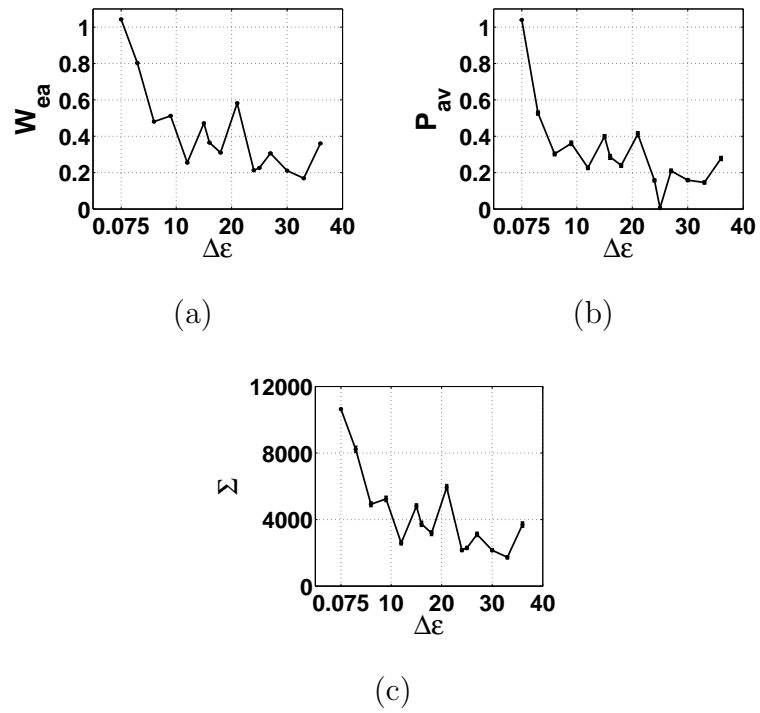
Fig. 2.4. Normal incidence, $\{P, Q\} = \{3, 3\}$, $f = 0.5$, and $d = \lambda/8$ as a function of dielectric contrast, $\Delta\epsilon$: (a) normalized transmitted electric energy, W_{ea}; (b) normalized transmitted power P_{av}; and (c) Σ. The calculated data points with error bars are shown.

nations with a fixed resolution. For example, when $\{P, Q\} = \{3, 3\}$, if the structure is composed of scatterers m_1 with probability $p = 0.5$ or the background material m_2 with probability $p = 0.5$, we have a total of 2^9 combinations. In the case of $f = 0.5$, the number of combinations is equal to the combination of 9 things taken 4 at a time without repetition. To examine the difference between a fixed filling factor and a fixed probability, we simulated the same parameter space but with the presence of each scatterer determined by $p = 0.5$ instead of $f = 0.5$. The results with a fixed probability are shown in Figs. 2.5(d) and (e). There are some differences between σ_C^2 in Fig. 2.5(a), for $f = 0.5$, and (d), for $p = 0.5$, and likewise for λ_1 in Figs. 2.5(b), for $f = 0.5$, and (e), for $p = 0.5$. We can observe that for $\Delta\epsilon = 3$, the variance of fields with a fixed p is larger than the result with a fixed f. This indicates that the contribution from the combinations lost due to a fixed f is appreciable. However, the $\Delta\epsilon$ points where the resonances occur are the same. The combinations with fixed f still provide a good prediction of the $\Delta\epsilon$ values that maximize σ_C^2.

The resolution of the binary aperiodic structure is also an important factor which may influence field control. We simulated structures with resolutions from $\{P, Q\} = \{3, 3\}$ to $\{20, 20\}$ with $f = 0.5$, and with all other parameters the same as the previous simulations. Figure 2.6(a) shows σ_C^2 as a function of resolution for $\Delta\epsilon = 11.38$. We observe that σ_C^2 varies nonlinearly with the resolution, and the case with $\{6, 6\}$ offers the greatest control. With higher resolution ($\{P, Q\} > \{10, 10\}$), only a relatively small change in total variance can be observed compared to that of the lower resolution cases. In general, one would anticipate that decreasing the size of the elements of the structure would lead to the homogenized regime, a loss of field control at the detector, and hence to reducing σ_C^2. It is likely that this is not observed in Fig. 2.6(a) because the measurements are made in the near field ($d = \lambda/8$)), so that even at the highest resolution used we still have not reached the homogenized material limit. While λ_1 has a similar appearance to σ_C^2, with a maximum when $\{P, Q\} = \{6, 6\}$, the ranks are almost independent of resolution. With a fixed size of 700×700 nm^2, we obtained numerical data as a function of background wavelength over the range 100
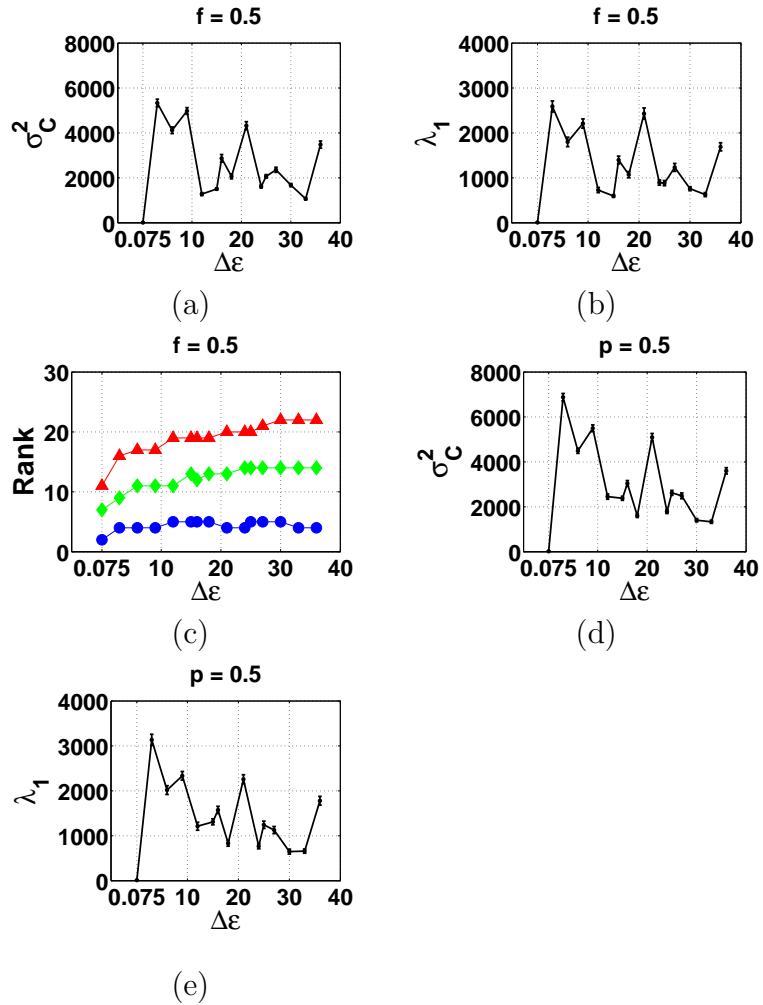
Fig. 2.5. Normal incidence and data as a function of $\Delta\epsilon$ for $\{P, Q\} = \{3, 3\}$ and $d = \lambda/8$ nm: (a) σ_C^2 with $f = 0.5$; (b) λ_1 with $f = 0.5$; (c) rank with thresholds of 1% (blue circle), $10^{-5}\%$ (green diamond), $10^{-10}\%$ (red triangle) with $f = 0.5$; (d) σ_C^2 with $p = 0.5$; and (e) λ_1 with $p = 0.5$. The calculated data points with error bars are shown in (a), (b), (d) and (e).
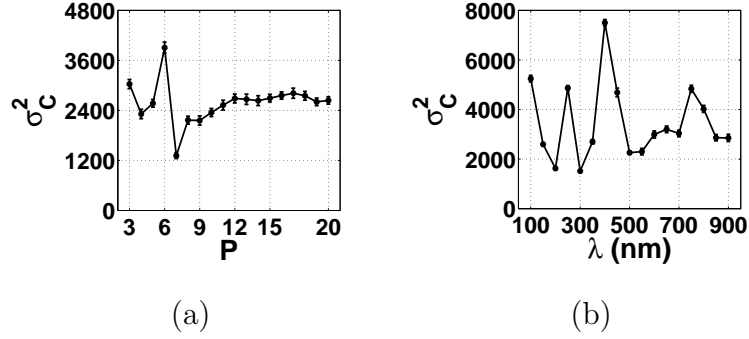
Fig. 2.6. Normal incidence, $\Delta\epsilon = 11.38$, $d = \lambda/8$, where $\lambda = 700$ nm, and $f = 0.5$: (a) σ_C^2 as a function of resolution $\{P, Q\}$, where $P = Q$; and (b) σ_C^2 plotted as a function of wavelength of the incident wavelength, λ, with $\{P, Q\} = \{3, 3\}$. The calculated data points with error bars are shown.

to 900 nm for $\Delta\epsilon = 11.38$, $\{P, Q\} = \{3, 3\}$, and $f = 0.5$. As shown in Fig. 2.6(b), σ_C^2 oscillates and shows strong resonant features as a function of wavelength. An incident wave with larger wavelength will enter a relatively finer (compared to the wavelength) binary nanostructure than that with smaller wavelength. This gives a somewhat similar situation to viewing σ_C^2 as a function of resolution.

2.4.2 Oblique Incidence - Dielectric Elements

To explore aperiodic element field control as a function of incident field wavefront, we consider an obliquely incident pane wave at an angle θ_i to the normal. Figure 2.7(a) shows σ_C^2 as a function of d for $\theta_i = \pi/6$, with error bars. The results are similar to the normal incidence case (Fig. 2.2(a)), with the largest variance closest to the structure ($d = \lambda/8$) and decreasing variance with increasing d. Although the general trend for σ_C^2 is similar for $\theta_i = 0$ and $\theta_i = \pi/6$, the magnitude is lower for the oblique incidence case. In addition, as for the normal incidence case, the rank decreases with increasing d and the influence of the degrees of freedom in controlling he eigenchannels diminishes. Figure 2.7(b) shows the influence of fill (f) on σ_C^2 for $d = \lambda/8$ and $\theta_i = \pi/6$ for $\{P, Q\} = \{3, 3\}$ and $\Delta\epsilon = 11.38$. As for the previous simulations, we round down
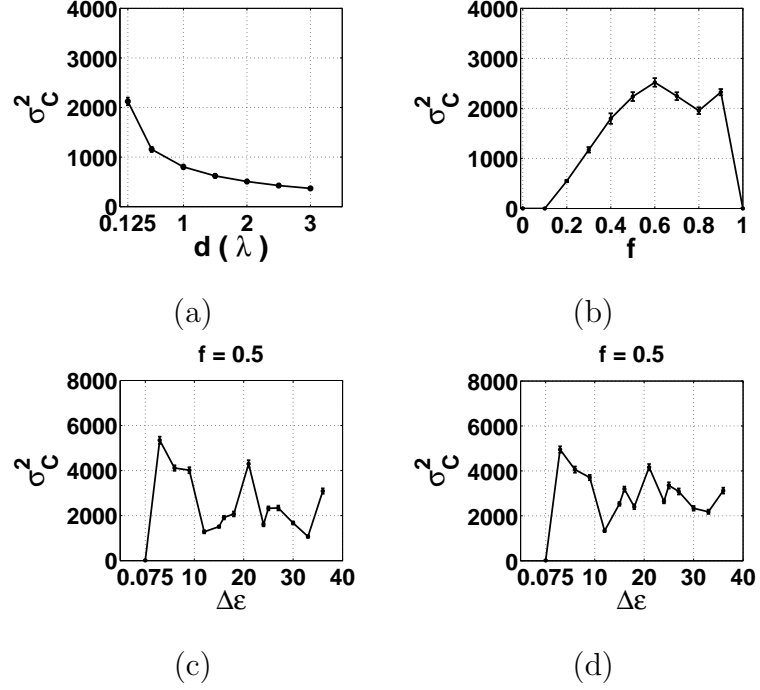
Fig. 2.7. σ_C^2 for oblique incidence with $\{P, Q\} = \{3, 3\}$: (a) $\theta_i = \pi/6$, $\Delta\epsilon = 11.38$, and $f = 0.5$ as a function of d: (b) $\theta_i = \pi/6$, $\Delta\epsilon = 11.38$, and $d = \lambda/8$ as a function of f; (c) $\theta_i = \pi/6$ for $f = 0.5$, and $d = \lambda/8$ as a function of $\Delta\epsilon$; and (d) $\theta_i = \pi/3$ for $f = 0.5$, and $d = \lambda/8$ as a function of $\Delta\epsilon$. The calculated data points with error bars are shown.

the number of scatterers for a particular filling factor. The shape of the $\sigma_C^2(f)$ curve is similar to that for normal incidence, but indicates slightly less control (smaller variance) linked to a reduction in energy at the detector plane. Consider now the influence of the dielectric constant. In Fig. 2.7(c) and Fig. 2.7(d), we plot σ_C^2 as a function of $\Delta\epsilon$ for $\theta_i = \pi/6$ and $\pi/3$, respectively, for $\{P, Q\} = \{3, 3\}$ and $f = 0.5$, with all other parameters the same as the previous simulations. Notice the trend to slightly lower σ_C^2 with further increase in θ_i. In Fig 2.7(c) and Fig 2.7(d), as for normal incidence, σ_C^2 increases with larger $\Delta\epsilon$, is maximum at $\Delta\epsilon = 3$ for both $\theta_i = \pi/6$ and $\theta_i = \pi/3$, and then reduces and oscillates with further increases in $\Delta\epsilon$. However, the variations in $\sigma_C^2(\Delta\epsilon)$ become less pronounced with increase in θ_i.

We calculate the normalized transmitted electric energy, W_{ea} in (2.9), and the normalized transmitted power, P_{av} in (2.10). Figures 2.8(a) and (b) give the results as a function of d. The detector line is perpendicular to the x-direction. With off-normal incidence, the x-directed Poynting vector and the energy at the detector on average increase with increasing d. We understand this in comparison with the normally incident results in Figs. 2.2(e) and (f) as being due to a substantial contribution from the incident field with oblique incidence. As we indicate before, only the scattered field can be controlled. Figure 2.8(c) gives the results for W_{ea} and Fig. 2.8(d) for P_{av} with $\theta_i = \pi/6$. The $\theta_i = \pi/3$ results are shown in Figs. 2.8(e) and (f). In Fig. 2.8, similar to the normal incidence result, W_{ea} and P_{av} deposited on the detector line with a fixed length oscillates with varying $\Delta\epsilon$ and show resonances at specific $\Delta\epsilon$ values that are relatively insensitive to incidence angle. Relative to normal incidence, the variations are smaller with increasing θ_i. In Figs. 2.7(c) and (d), the variations in $\sigma_C^2(\Delta\epsilon)$ diminish and bear a resemblance to those for the energy in Figs. 2.8(c) and (e). Reduced transmitted energy depresses the variance. However, we should note that while low energy and power imply a reduction in σ_C^2, the converse is not necessarily the case. There is a tendency for high energy to correlate with peaks in σ_C^2, but a comparison of Figs. 2.7(c) and (d) with Figs. 2.8(c) and (e) shows that the variance and energy variations (notably the peaks) do not track perfectly.

Both the normal and oblique incidence cases studied indicate a similar number of controllable channels, i.e., that there is weak dependence on incidence angle. We can therefore conclude that the measures we have applied provide guidance regardless of the incident field.

2.4.3 Metal (Plasmonic) Elements

With the view that strongly scattering media may provide more control opportunities, we consider a model for metals in the optical regime where the real part of the dielectric constant is negative. For simplicity, we neglect loss and hence set the
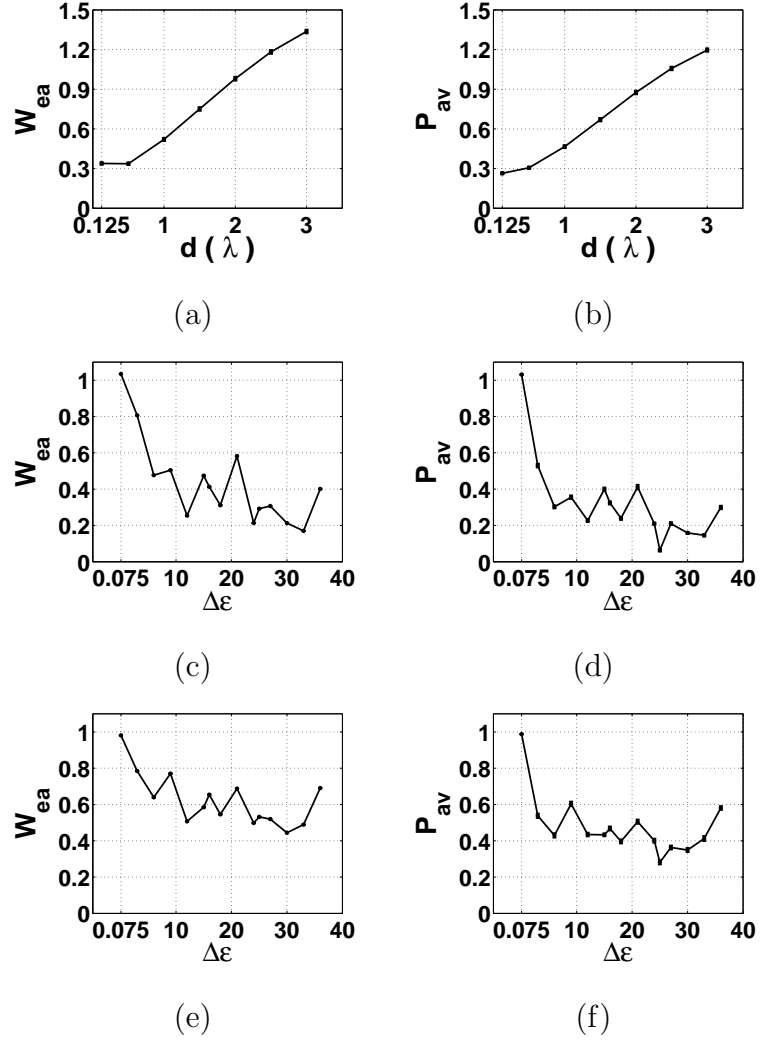
Fig. 2.8. With $\{P,Q\} = \{3,3\}$, $f = 0.5$: (a) W_{ea} for $\theta_i = \pi/6$ and $\Delta\epsilon = 11.38$ as a function of distance to the detector line, d; (b) P_{av} for $\theta_i = \pi/6$, and $\Delta\epsilon = 11.38$ as a function of d; (c) W_{ea} for $\theta_i = \pi/6$ and $d = \lambda/8$ as a function of dielectric contrast, $\Delta\epsilon$; (d) P_{av} for $\theta_i = \pi/6$ and $d = \lambda/8$ as a function of $\Delta\epsilon$; (e) W_{ea} for $\theta_i = \pi/3$, and $d = \lambda/8$ as a function of $\Delta\epsilon$; and (f) P_{av} for $\theta_i = \pi/3$ and $d = \lambda/8$ as a function of $\Delta\epsilon$. The calculated data points with error bars are shown.

imaginary dielectric constant to zero. Figure 2.9(a) shows the normalized transmitted electric energy, W_{ea}, and Fig. 2.9(b) the normalized transmitted power, P_{av}, as a function of $\Delta\epsilon$. Both W_{ea} and P_{av} are relatively small compared with the positive dielectric constant cases due to the strong reflection associated with the negative dielectric constant. We should note is this reduced energy picture may differ with other geometries, most notably, those that permit wave guiding used in earlier aperiodic structures [4], in particular, the metal-insulator-metal mode [51,52]. In Fig. 2.9(c), we plot σ_C^2 as a function of $\Delta\epsilon$. Small oscillations can observed as the dielectric constant becomes more negative. This can be predicted by the energy and power results in Fig. 2.9(a) and (b), and reduced transmitted energy brings about a decrease in σ_C^2. The largest eigenvalue, λ_1, gives similar results to Fig. 2.9(c). We conclude that for the binary aperiodic structure of Fig. 2.1, use of a negative dielectric constant does not provide as many controllable channels as a positive dielectric constant, and we attribute this to a reduction in transmitted energy.

2.5 Field Statistics

The field density function on the detector line in Fig. 2.1 provides another measure for aperiodic elements that we consider. The computed probability density functions from the numerical data used to produce Fig. 2.5 for different $\Delta\epsilon$ are compared with analytic density functions. The numerical E_z for multiple structure arrangements provides the data to generate the field density function, as well the intensity density function.

We define $\phi_{R,I}$, A, I as the real and imaginary part of the field (E_z in our case), the field amplitude, and the intensity, respectively. For zero-mean circular Gaussian

(a)

(b)

(c)
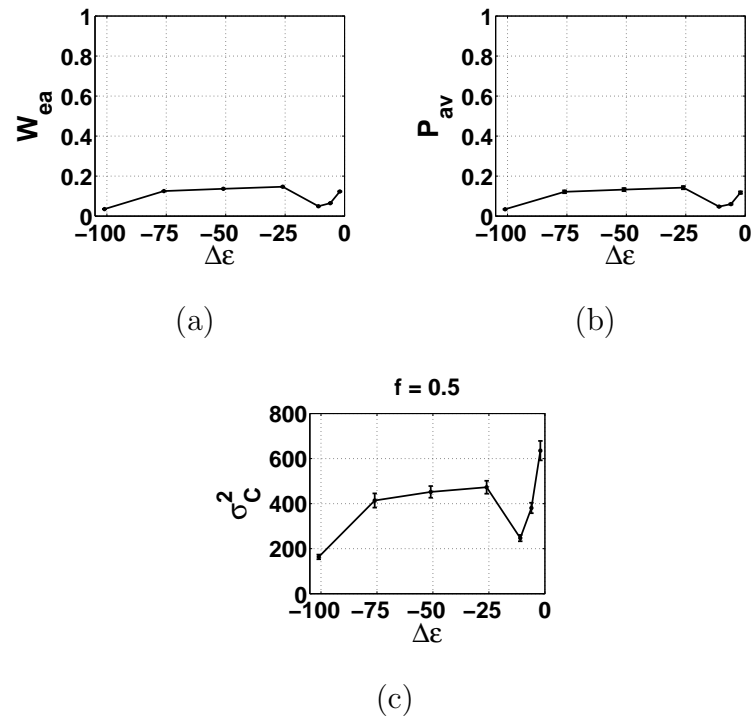
Fig. 2.9. Normal incidence for $\{P, Q\} = \{3, 3\}$, $f = 0.5$, and $d = \lambda/8$: (a) $W_{ea}(\Delta\epsilon)$; (b) $P_{av}(\Delta\epsilon)$; and (c) $\sigma_C^2(\Delta\epsilon)$. The calculated data points with error bars are shown.

field statistics, when the field can be considered as the sum of a large number of independent random phasors, the corresponding probability density functions are [53]

$$p(\phi_{R,I}) = \frac{1}{\sqrt{2\pi\sigma^2}}e^{-\phi_{R,I}^2/(2\sigma^2)} \tag{2.14}$$

$$p(A) = \frac{A}{\sigma^2}e^{-A/(2\sigma^2)} \tag{2.15}$$

$$p(I) = \frac{1}{2\sigma^2}e^{-I/(2\sigma^2)}, \tag{2.16}$$

Gaussian field amplitude, Rayleigh magnitude, and negative exponential intensity distributions, respectively. Using a normalization scheme ($\hat{\phi}_{R,I} = \phi_{R,I}/\sqrt{\langle A^2 \rangle}$, $\hat{A} = A/\sqrt{\langle A^2 \rangle}$, and $\hat{I} = I/\langle I \rangle$), the probability density functions for normalized field, amplitude, and intensity can be written as [8,9]:

$$p(\hat{\phi}_{R,I}) = \frac{1}{2}e^{-\pi\hat{\phi}_{R,I}^2/4}, \tag{2.17}$$

$$p(\hat{A}) = 2\hat{A}e^{-\hat{A}^2}, \tag{2.18}$$

$$p(\hat{I}) = e^{-\hat{I}}. \tag{2.19}$$

Consider now $\Delta\epsilon = 9$, which has large σ_C^2 in Fig. 2.5(a). The computed probability density functions of the normalized total field in Fig. 2.10(a) and intensity in Fig. 2.10(b) conform nicely to the zero-mean Gaussian field and negative exponential intensity density functions, respectively. We interpret this agreement at relatively large dielectric constant with fixed scatterer size as due to a substantial number of contributing random phasors, associated with multiple scatter. However, when the strength of the scatter becomes very large, as in the extreme case of Fig. 2.11, where $\Delta\epsilon = 100$, the Gaussian distribution no longer fits the probability density function well (see the green dashed lines in Fig. 2.11). In this case, the strong scatter is reducing the number of contributing phasors. This occurs in Anderson localization, and the field density function describing this phenomenon has been found to be circular Bessel [9]. Such a density function can be used to describe the results of Fig. 2.11.

We assume that the total field, ϕ, is modeled by the sum of N random phasors [8],

$$\phi = \sum_{n=1}^{N} \phi_n = \sum_{n=1}^{N} a_n e^{j\theta_n} = Ae^{j\theta}, \tag{2.20}$$
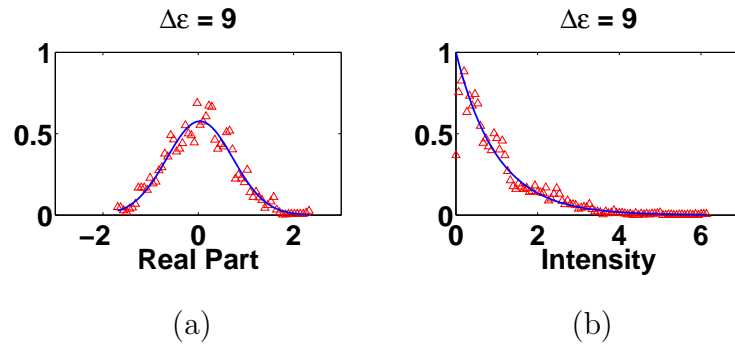
Fig. 2.10. Near-field probability density functions for $d = \lambda/8$, $\{P, Q\} = \{3, 3\}$, $\Delta\epsilon = 9$, and $f = 0.5$: (a) normalized real part of the total field ϕ (E_z, referring to Fig. 2.1) on the detector line; and (b) corresponding intensity data. Note that the field is captured by a zero-mean Gaussian density function, and hence the intensity distribution is negative exponential, as the blue line fits to the numerical data (triangles) show.
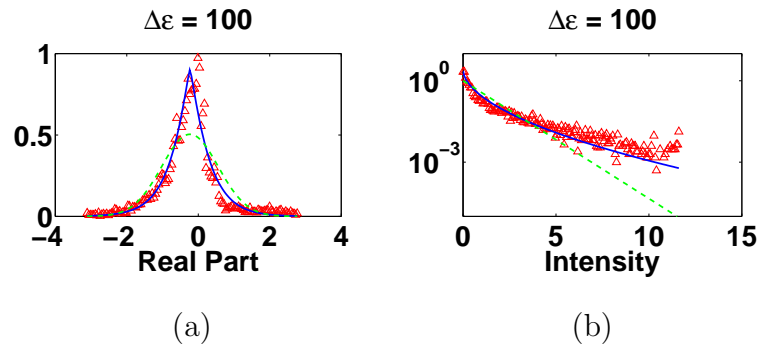
Fig. 2.11. Density function data for $d = \lambda/8$, $\{P, Q\} = \{3, 3\}$, $\Delta\epsilon = 100$, and $f = 0.5$: (a) normalized real part of the total field ϕ; and (b) the corresponding intensity density function. The green dashed curves in (a) and (b) are, respectively, Gaussian and negative exponential fits. The blue solid curves show the better fit to the numerical data using a circular Bessel density function.

that the amplitudes and the phases are independent of each other, and that all phases are uniformly distributed over 2π, resulting in circular statistics in the complex plane. We also assume that the fluctuations in N can be described by a probability mass function that is the negative binomial distribution,

$$p(N) = \binom{N + \alpha - 1}{N} \frac{(\langle N \rangle / \alpha)^N}{(1 + \langle N \rangle / \alpha)^{N+\alpha}}, \tag{2.21}$$

where $\langle N \rangle$ is the mean value of N and α is a positive real real number. The shape of this distribution is governed by the parameter α. When $\alpha \gg 1$, it is centered around its mean, $\langle N \rangle$. For sufficiently large $\langle N \rangle$, the central limit theorem applies, leading to Gaussian statistics. When $\alpha \ll 1$, it is peaked at $N = 0$ and then decreases as N increases, which is the case of circular Bessel statistics.

The probability density functions of normalized field and intensity for circular Bessel statistics are derived to be [8]

$$p(\hat{\phi}_{R,I}) = \frac{2}{\sqrt{\pi}\Gamma(\alpha)} \alpha^{(\alpha+1/2)/2} (\hat{\phi}_{R,I}^2)^{(\alpha-1/2)/2} K_{\alpha-1/2}\left(2\sqrt{\alpha\hat{\phi}_{R,I}^2}\right) \tag{2.22}$$

$$p(\hat{I}) = \frac{2\alpha}{\Gamma(\alpha)} (\alpha\hat{I})^{(\alpha-1)/2} K_{\alpha-1}(2\sqrt{\alpha\hat{I}}), \tag{2.23}$$

where Γ is the gamma function and K is the modified Bessel function of the second kind. Equations (2.23) and (2.23) are also effective for Gaussian statistics, when α approaches infinity.

In Figs. 2.11(a) and (b), the blue lines show that the numerical field and intensity data for $\Delta\epsilon = 100$ can be nicely fit with the circular Bessel distribution, (2.23) and (2.23). This reveals that a small number of contributing phasors is involved in forming these near-field statistics. From Figs. 2.10 and 2.11, we conclude that the fields are describable as Gaussian below some scattering strength that is less than $\Delta\epsilon = 100$ and greater than $\Delta\epsilon = 9$ for the geometry considered.

In addition, from (2.3), the total field ϕ is the summation of the incident and scattered fields. For weak scatter (small $\Delta\epsilon$), the amplitudes of scattered fields are generally much smaller than those of the incident field under weak scatter, such that
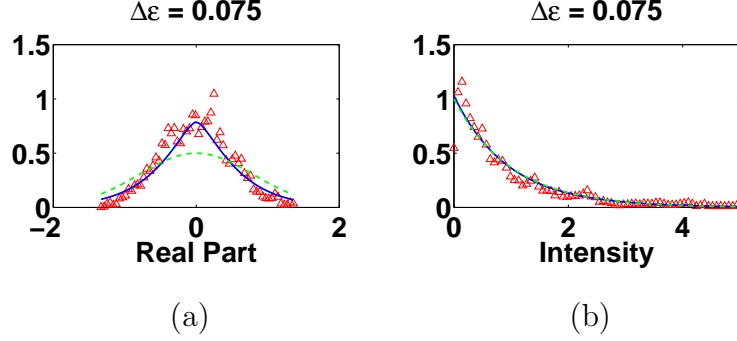
Fig. 2.12. Residual field density function data for $d = \lambda/8$, $\{P, Q\} = \{3, 3\}$, $\Delta\epsilon = 0.075$, and $f = 0.5$: (a) normalized real part of the residual field $\delta\phi$; and (b) the corresponding intensity density function. The green dashed curves in (a) and (b) are, respectively, Gaussian and negative exponential fits. The blue solid curves show the better fit to the numerical data using a circular Bessel density function.

the total field ϕ can not be circular with zero mean. The total field ϕ can be written as the sum of the mean field $\langle\phi\rangle$ and the residual field $\delta\phi$, giving

$$\phi(\mathbf{r}) = \langle\phi(\mathbf{r})\rangle + \delta\phi(\mathbf{r}), \qquad (2.24)$$

where the averaging is over the random arrangements and $\mathbf{r}$ indicates the position at the detector. Earlier work has shown that the residual field $\delta\phi$ can develop an approximately zero-mean character when the scatter is too weak for the total field to exhibit such statistics [8]. Figures 2.12(a) and (b) show the probability density functions of the normalized real part and intensity of the residual field, $\delta\phi$, respectively, for weak scatter ($\Delta\epsilon = 0.075$). The results fit the circular Bessel statistics better than the zero-mean Gaussian and confirm the zero-mean statistics for the residual field $\delta\phi$.

2.6 Conclusion

We provided a multivariate statistical analysis of binary aperiodic scattering elements based on a principal component analysis, along with information on the character of the field density function, to evaluate the degrees of freedom available for controlling the near-field through to the far-field response. The eigen-decomposition

of the field covariance matrix gives us a measurable number to compare the variances of fields (σ_C^2) that nanostructures can support in different cases.

As expected, this measure shows that field control diminishes with increasing distance to the detector, i.e., $\sigma_C^2(d)$ is a decreasing function of d. We considered spatial Fourier domain data, but far-field results with the small (λ) spatial support of the detector line precluded observation of equivalent of the propagating mode limit found in earlier work [6,25]. A larger fill factor provides more scatterers, more degrees of freedom, and hence more control, but all control is lost with complete fill. We find fill fractions of 0.5-0.9 are best for the binary dielectric structures we studied. We found that strong scatter does not always support more degrees of freedom due to the loss of transmitted energy. Small energy at the detector cannot support a large σ_C^2. In the cases studied, dielectric constant differences from the background in the range of 3-9 provide large σ_C^2, which turns out to be fortuitous given the number of materials encompassed at optical frequencies. While the case of metals in the binary structures we considered was not favorable, due to the low energy at the detector, other waveguide-type structures will likely change this position. Fixing the scatterer size and increasing the discretization provided more freedom, but above a certain discretization, similar σ_C^2. We expect that the homogenized regime will be reached with increasing discretization, with concomitant loss of control, but our data did not extend to this regime. Our metrics appear quite insensitive to the incident phase front (angle of incidence), suggesting general conclusions can be made from, for example, the normal incidence case.

The weakly and strongly scattering aperiodic element fields were found to be well described by circular Bessel statistics, and intermediate scatter resulted in Gaussian fields. The regime where zero-mean circular Gaussian field statistics hold appears to be the domain where there is more field control (and more independent phasors), and presumably where this class of aperiodic elements is optimal.

The results we have presented provide design guidelines to optimize different parameters within bounded ranges. This can benefit applications such as imaging,

microscopy and spatial control. While we have considered binary aperiodic elements, there are inferences related to continuously varying aperiodic materials one might make. For example, each binary arrangement is similar to having scatterers at random locations, i.e., random media where the locations of the scatterers can be viewed as being drawn from a density function. Another continuous optimization variant of the binary structure we considered would have each pixel with a continuously varying dielectric constant, or the dielectric constant fixed and the boundary of each scatter parameterized in an optimization framework. Conclusions from our studies related to fill factor and changes in dielectric constant could help guide the design process in these situations.

3. THE PHYSICAL BASIS OF ENHANCED OPTICAL PRESSURE ON A STRUCTURED SURFACE

It has been proposed that structuring a metal surface can substantially increase the optical pressure over that possible with a planar interface. While this was presented as being associated with a plasmon wave resonance in nanostructured cavities, the physical mechanism by which the pressure is increased has remained unclear. Based upon the forces on the mirrors of a one-dimensional Fabry-Perot cavity, we show that the force on one mirror in an asymmetric arrangement can be increased relative to the other, and relate the pressure to the quality factor in the cavity and the mirror properties. Importantly, we also show that the sum of the pressures on both mirrors increases through asymmetry and with quality factor. Using cavity quality factor as a measure, the one-dimensional Fabry-Perot cavity pressure results are related to pressure enhancement with a structured metal surface. The enhanced pressure phenomenon is explained as being due to an array of asymmetric optical cavities formed on the surface. With this understanding guiding the design of structured metallic and dielectric materials, more than an order of magnitude increase in the optical pressure is possible. Consequently, the relatively weak optical force can become more effective in control and propulsion applications.

3.1 Introduction

Radiation pressure was theorized [54] and measured [55] more than one century ago, and optical force concepts developed since the advent of the laser have led to optical tweezers [56] and extensive interest in optical traps and condensates [57]. There has been substantial work done related to forces within optical cavities and on the cavity mirrors, primarily related to sensitivity and cooling [58–61]. The development

of sensitive interferometers [62] have allowed the detection of gravitational waves [63]. Cavity dynamics concepts are based on the mirror radiation pressure being $P = 2\hbar k I$, with each photon carrying a momentum $\hbar k$ and I being the optical intensity measured in photons/$(\mathrm{m}^2 \cdot \mathrm{s})$, given P in N/m^2, and the factor of two is from the assumption of perfect reflection [64]. This is entirely consistent in the appropriate limit with the classical picture from Maxwell [54], where $P = S(1 + |\Gamma|^2)/c$, with Γ the field reflection coefficient. Clearly, increasing I or the incident Poynting vector by increasing the cavity quality factor (Q) will increase the pressure on the mirror. However, $|\Gamma| = 1$ leads to a maximum value of $P = 2S/c$.

The force density in homogenized media can be obtained from the field solution, and this leads to a means to calculate the force on a medium [65,66], the pressure on a slab [12,67], and with photonic crystal mirrors [68]. With such an approach involving a numerical solution for the fields in the material, leading to the force density and hence pressure, the possibility of increasing the pressure by more than an order of magnitude over $2S/c$ with a nanostructured Au surface has been presented [11]. This result could be profoundly important in applications, but the physical basis of the effect related to a plasmon wave resonance has remained unclear. We present an understanding based on an asymmetric 1D Fabry-Perot cavity and the increase in the total pressure on both mirrors at resonance. This leads to a means to achieve pressure enhancement with a variety of dielectric and metallic materials for remote control, propulsion, and cavity optomechanics applications. The resulting change in the mathematical picture of pressure [54] should provide a basis for new directions in optomechanics for the physical sciences.

We explain optical pressure enhancement on a surface by considering the mirror pressures in the 1D Fabry-Perot cavities shown in Figs. 3.1(a) and (b), which we relate to cavity Q and the MIM-mode cavities in Figs. 3.1(c) and (d), all in a free space background. Figure 3.1(a) shows a symmetric Fabry-Perot cavity containing two identical slab mirrors (M$_1$ and M$_2$) with thickness t, and a cavity length d, defined as the mirror separation. Figure 3.1(b) shows an asymmetric Fabry-Perot
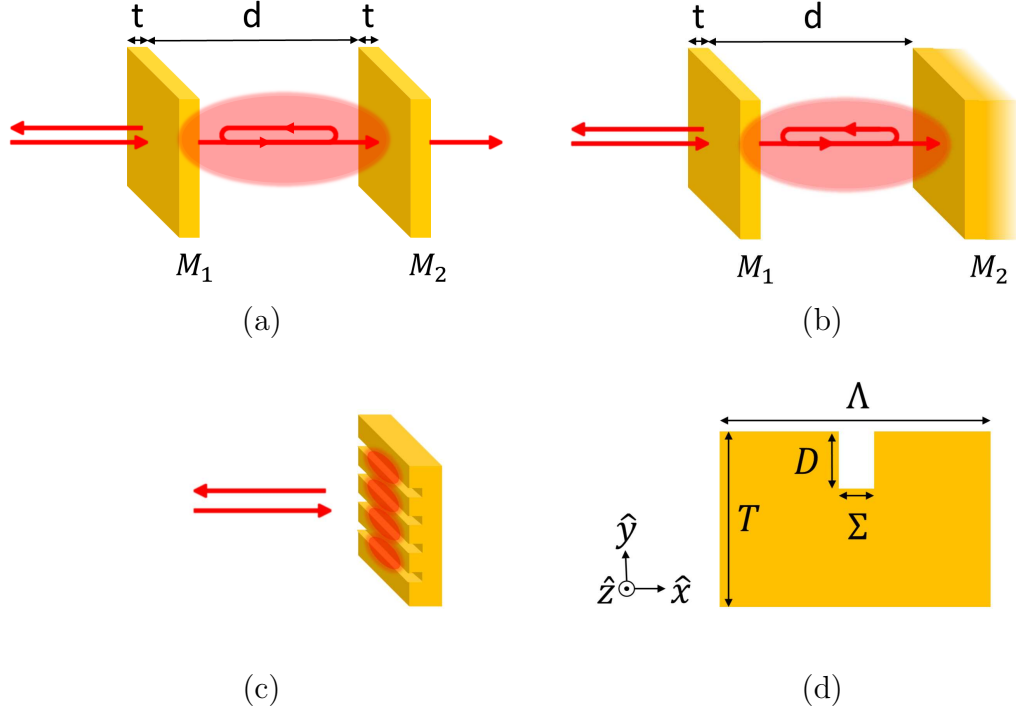
Fig. 3.1. Optical cavities that enhance the radiation pressure. (a) A symmetric Fabry-Perot cavity. The mirrors M_1 and M_2 are two identical slabs with thickness t separated by d. (b) An asymmetric Fabry-Perot cavity. M_1 is a slab with thickness t and M_2 is a semi-infinite mirror placed d away from M_1. (c) A nanostructured slot cavity array in a metal. (d) Profile of a unit cell of the periodic nanostructured slot cavity in (c). A normally-incident plane wave of wavelength 633 nm and Au with artificially adjusted loss are assumed, as described in Table 3.1.

cavity with M_1 having thickness t and the semi-infinite M_2 placed a distance d away from M_1. Figure 3.1(c) shows a nanostructured slot cavity array and the profile of each slot is shown in Fig. 3.1(d). With an incident field having H_z, the lowest order MIM waveguide mode (E_x, E_y, H_z) can be excited, by virtue of the metal dielectric constant ($\epsilon = \epsilon' + i\epsilon''$ with $\epsilon' < -1$, assuming a free space background) [51]. We present radiation pressure simulation results for 1D cavities in Figs. 3.1(a) and (b) and use these to build physical insight into the influence of structures like Figs. 3.1(c) and (d) to enhance the pressure.

Table 3.1.

The cavity mirror material parameters used in the calculations related to Figs. 3.1(a) and (b). Nomenclature: symmetric Fabry-Perot (SFP), cases 1 (SFP1) and 2 (SFP2), as in Fig. 3.1(a); asymmetric Fabry-Perot (AFP), cases 1-3, as in Fig. 3.1(b). The dielectric constant assumed for Au is $\epsilon_{Au} = -11.82 + i1.23$ at a wavelength of 633 nm, and in all cases, $\epsilon'_{M1} = \epsilon'_{M2} = -11.82$. The imaginary part of the dielectric constant for each mirror, ϵ''_{M1} and ϵ''_{M2}, is varied as indicated to adjust the confinement and dissipation in the cavities.

	t_{M_1}	ϵ''_{M_1}	t_{M_2}	ϵ''_{M_2}
SFP1	30 nm	0, 0.1, 0.2, $\cdots$, 1	Same as M_1	
SFP2	50 nm	and 1.23 $(\Im\{\epsilon_{Au}\})$		
AFP1	30 nm		Semi-infinite	1.23 $(\Im\{\epsilon_{Au}\})$
AFP2	50 nm			
AFP3	50 nm			0.1

3.2 Methodology

The separable problems in Figs. 3.1(a) and (b) can be solved analytically, and we do so for excitation with a single, normally incident plane wave from the left, allowing the force densities in the mirrors and hence the pressure to be obtained. Using impedance transformation, the field reflection coefficient, S_{11} (with scattering parameter notation), can be found at the left interface of M_1 [69]. This circumvents the need to define a specific cavity boundary and some cavities of interest have no transmission. Using the recursive from of the field transmission matrix, the fields are found in the cavity and within the mirrors [69]. The fields in the mirrors lead to the force density and hence the pressure. The force density expression we utilize here, originally from Einstein and Laub [70], has been derived and used by others [12,65,66,71], and was also used to present the idea of enhanced pressure in structured material [11]. We assume that no magnetic material response exists in the source-free case. Consequently, the force density within the material media assuming $\exp\left(-i\omega t\right)$ is

$$\langle \mathbf{f} \rangle = (\hat{\mathbf{e}} \times \hat{\mathbf{h}})\frac{\mu_0\epsilon_0\omega}{2}\Im\{\chi_E E(\mathbf{r})H^*(\mathbf{r})\} + \frac{\epsilon_0}{2}\Re\{(\chi_E E(\mathbf{r})\hat{\mathbf{e}}\cdot\nabla)(\hat{\mathbf{e}}E^*(\mathbf{r}))\} \quad (3.1)$$

where $\hat{\mathbf{e}}$ and $\hat{\mathbf{h}}$ are unit vectors indicating the direction of the electric and magnetic field phasors, E and H, at position $\mathbf{r}$, respectively, χ_E is the electric susceptibility, $\Re\{\cdot\}$ is the real part and $\Im\{\cdot\}$ the imaginary part, μ_0 is the free space permeability and ϵ_0 is the free space permittivity. We define the time-averaged force density due to the first term in (3.1) as $\langle \mathbf{f_R} \rangle$, where the nomenclature implies that this is the radiation pressure for a planar surface with normal incidence, the usual mirror picture, and the other term due to the gradient of the field as $\langle \mathbf{f_G} \rangle$.

We relate the radiation pressure to the cavity Q. With the linear and isotropic relationships $\mathbf{D} = \epsilon_0\epsilon\mathbf{E}$ and $\mathbf{B} = \mu_0\mathbf{H}$, in frequency domain and where $\mathbf{D}$ is the electric flux density and $\mathbf{B}$ the magnetic flux density, it is possible to separate electromagnetic field energy into stored energy and lost energy [72]. Under the assumption that

dispersion can be neglected, so $\partial\epsilon/\partial\omega = 0$, the time-averaged stored energy surface density (J/m^2) is

$$W \;=\; \frac{1}{4}\int_l \left[\epsilon'\epsilon_0|E(\mathbf{r})|^2 + \mu_0|H(\mathbf{r})|^2\right]\,\mathrm{d}l, \tag{3.2}$$

where l is the spatial variable perpendicular to the mirrors. Likewise, the time-averaged power dissipation surface density (W/m^2) is

$$P_d \;=\; \frac{\omega}{2}\int_l \epsilon_0\epsilon''|E(\mathbf{r})|^2\mathrm{d}l. \tag{3.3}$$

The integrations in (3.2) and (3.3) are over the mirrors and the intervening space (free space in the situations of Figs. 3.1(a) and (b)), and for M_2 in the asymmetric cavity case, the integral in that mirror is over 20δ, with δ the skin depth (e^{-1} of the field at the surface).

The Q can be decomposed into unloaded (accounting for loss within the cavity, Q_U) and loaded (describing the radiative loss contribution, Q_L) as

$$\frac{1}{Q} \;=\; \frac{1}{Q_U} + \frac{1}{Q_L}, \tag{3.4}$$

where

$$Q_U = \omega_0\frac{W_0}{P_d} \quad \text{and} \quad Q_L = \omega_0\frac{W_0}{S_r + S_t}, \tag{3.5}$$

with ω_0 the resonant circular frequency, W_0 the total (electric plus magnetic) energy in the cavity at resonance from (3.2), P_d the power dissipated within the cavity at resonance from (3.3), and S_r and S_t the reflected and transmitted Poynting vector magnitudes, respectively, at resonance. With high cavity finesse and use of a Lorentzian line model [73, 74],

$$1 - |S_{11}(\omega)|^2 \;=\; \frac{1 - |S_{11}(\omega_0)|^2}{1 + 4\frac{(\omega_0-\omega)^2}{\Delta\omega^2}}, \tag{3.6}$$

and an estimate of Q is

$$Q_\omega = \frac{\omega_0}{\Delta\omega}, \tag{3.7}$$

where $\Delta\omega$ is the half-power bandwidth and the subscript ω indicates this frequency response measure (with a high Q approximation). Measuring S_{11} and use of (3.7) to determine Q circumvents the need to artificially define cavity boundaries.

3.3 Results

Figure 3.2 shows our pressure results for the 1D cavities of Figs. 3.1(a) and (b) at resonance. We designate symmetric (Fig. 3.1(a)) and asymmetric (Fig. 3.1(b)) Fabry-Perot cavity cases through the labels SFP and AFP, respectively. In all calculations, the magnitude of the Poynting vector of the normally incident plane wave on the cavity is 1 W/m^2, and the free space wavelength is $\lambda_0 = 633$ nm. The mirror dielectric constants used are presented in Table 3.1 and based on Au, with the loss adjusted. We vary only the material loss and thickness to adjust the confinement and dissipation in the cavities. The shortest resonant cavity length was determined from the minimum $|S_{11}|$ as d is adjusted, and all results are for this condition. For the 1D cavities, only $\langle \mathbf{f_R} \rangle$ contributes to the pressure.

Figure 3.2(a) shows the radiation pressure on M$_2$, P_{M_2}, as a function of ϵ''_{M_1}, the imaginary part of the dielectric constant for M$_1$. In all cases, the pressure decreases with increasing ϵ''_{M_1} and the maximum enhancement occurs when M_1 is lossless. Note that the asymmetric cavity can provide a much larger pressure enhancement than the symmetric case by reducing the material loss in M_2 (AFP3), which can be understood from $P = S(1 + |\Gamma|^2)/c$ with $|\Gamma| \sim 1$. Changing ϵ''_{M_1} has an impact on the coupling between the incident wave and the cavity, so both Q_U and Q_L are varied, and the stored energy in the cavity varies. In order to compare the relationship between pressure and Q for the simple Fabry-Perot cavities of Figs. 3.1(a) and (b), we plot P_{M2} as a function of Q calculated from (3.4), with use of (3.5) and the cavity energy determined from (3.2) and the power dissipation from (3.3), in Fig. 3.2(b). A fit (orange line) in Fig. 3.2(b) makes the linear relationship between pressure and Q clear. Figure 3.2(c) shows P_{M_2} as a function of Q_ω, estimated from (3.7), which has a nonlinear relationship to pressure. However, the general trend between pressure and both Q and Q_ω are consistent. The nonlinear character in Fig. 3.2(c) appears at lower values of Q_ω and can be attributed to the breakdown of the high-Q approximation. With high Q_ω, the results in Fig. 3.2(c) still differ a little from those in
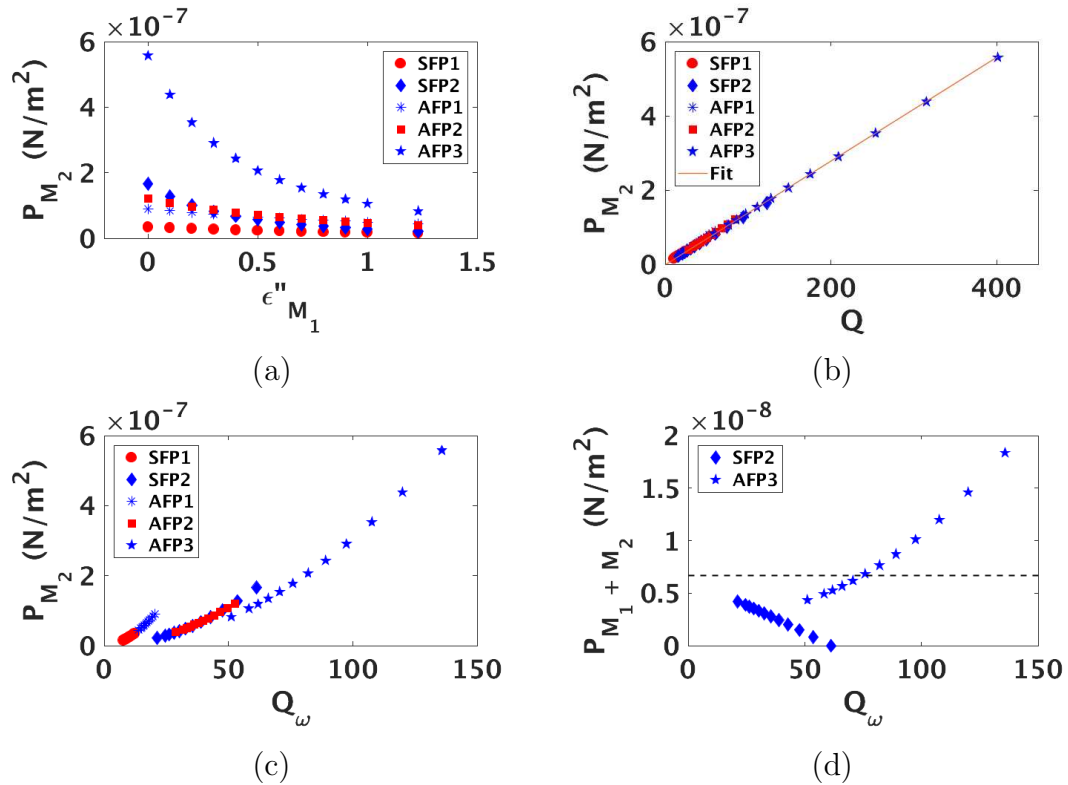
Fig. 3.2. (a) Radiation pressure P_{M_2} on M_2 as a function of ϵ''_{M_1} for examples of symmetric and asymmetric Fabry-Perot cavities with the parameters given in Table 3.1. (b) P_{M_2} on M_2 as a function of Q from (3.4), with a linear fit (orange line). (c) P_{M_2} as a function of Q_ω from (3.7). (d) Net pressure, $P_{M_1+M_2}$, on M_1 and M_2 as a function of Q_ω. The dashed line shows the value of the maximum pressure on a perfect mirror when the magnitude of the incident power density is 1 W/m^2. A resonant asymmetric cavity can support larger pressure enhancement than a perfect reflecting (anti-resonant) surface.

Fig. 3.2(b) because the cavity boundaries were (artificially) described at the outside of the mirror surfaces in determining both W_0 and Q (in Fig. 3.2(b)), while use of the reflection coefficient in (3.6) in determining Q_ω from (3.7) did not require a cavity boundary to be defined. We conclude then that Q_ω provides a suitable measure to investigate cavity mirror pressure. Figure 3.2(d) shows the net pressure on M_1 and M_2, $P_{M_1} + P_{M_2} = P_{M_1+M_2}$, for SFP2 and AFP3, the higher Q examples of symmetric and asymmetric Fabry-Perot cavities, respectively. When a symmetric Fabry-Perot cavity is resonant, the forward and backward waves within the cavity have approximately the same amplitude. Therefore, for a symmetric Fabry-Perot cavity, the pressure on M_1 is almost the same as P_{M_2} but in the opposite direction, causing $P_{M_1+M_2}$ to be approximately zero. This can be observed from the diamond symbols (SFP2) in Fig. 3.2(d) as Q_ω increases. On the other hand, with asymmetric mirrors, P_{M_2} is slightly larger than the pressure on M_1, leading to an increasing $P_{M_1+M_2}$ with increase in Q_ω, as evidenced by the star symbols in Fig. 3.2(d). The dashed line in Fig. 3.2(d) shows the maximum pressure on a perfect mirror based on $P = S(1 + |\Gamma|^2)/c$ when $S = 1$ W/m^2 and $\Gamma = 1$. From the AFP3 case in Fig. 3.2(d), given by the stars, it is clear that $P_{M_1+M_2}$, enhanced by the cavity Q, can exceed the maximum pressure on a perfect mirror $(2S/c)$ by 3 times (with the same power incident on the cavity). A key point in the results of Fig. 3.2 is that at the first resonance, $P_{M_1+M_2}$ is largest when the reflection coefficient at the left of M$_1$ ($|S_{11}|$) is a minimum. On the contrary, the maximum pressure based upon $S(1 + |\Gamma|^2)/c = 2S/c$ occurs when the reflection coefficient is maximum. The idea that higher reflection produces larger pressure has led to the use of highly reflecting surfaces achieved with distributed Bragg reflectors or photonic crystals. Our results indicate, quite differently, that a resonant asymmetric cavity can provide even larger pressure enhancement than the conventional limit. The asymmetric cavity total pressure in Fig. 3.2(d) provides a basis to understand the pressure enhancement in the slot cavity array of Fig. 3.1(c), as we show.

To obtain the fields and the corresponding radiation pressure in the nanostructured slot cavity in Fig. 3.1(c), we use a frequency domain finite element method

(FEM) to obtain the numerical field solutions [49]. Port boundaries are used in this 2-D model to extract S_{11} and placed $5\lambda_0$ above and below the structure in Fig. 3.1(d). To avoid singularities in the numerical simulations, the corners of each slot are rounded with radius of 1 nm. A numerical convergence study was performed. The maximum mesh element size in the scattering material is $\lambda_0/200$, sufficient to ensure the accuracy of the force density solutions. The slot depth, D, and width, Σ, are variables and the period is set to $\Lambda = 400$ nm and thickness to $T = 200$ nm. With a period of $\Lambda = 400$ nm, only the zeroth-order (normal) scattered plane wave propagates. We fix Σ and vary D to determine the resonant depth from the minimum of $|S_{11}|$.

The results for the slot resonant D as a function of Σ, labeled by the (red) diamonds, are shown on the right axes in Figs. 3.3(a) and (b). A reducing slot width results in a decreasing slot depth for the first resonance. We apply (3.7) to estimate Q_ω for the slot cavity, and the results are shown in Fig. 3.3(a) by the (black) triangles. Note that Q_ω increases with decreasing Σ, which can be understood by the cavity reflection coefficient at the top of the slot increasing as Σ is reduced, thereby increasing the lifetime of the guided-wave resonance in the slot and hence the Q_L. The numerical field solutions are used in (3.1) to find the force density, and this is integrated over the support of the material within the unit cell and divided by Λ to form the pressure, with the results given by the (black) asterisks for each value of Σ in Fig. 3.3(b). The general trends in Figs. 3.3(a) and (b) are that both Q_ω and pressure decrease with increasing slot width (at resonance). The pressure results for the slot cavities in Fig. 3.3(b) are consistent with the asymmetric 1D Fabry-Perot cavity results of Fig. 3.2(d) for AFP3, where the pressure increases with Q_ω. The anomalous pressure result for the smallest Σ in Fig. 3.3(b) occurs because of the small slot size and the reduced interaction between the field and the material.

Figure 3.3(c) shows the pressure as a function of Q_ω for the slot structures. Unlike the 1D Fabry-Perot cavities, the gradient force term, $\langle \mathbf{f_G} \rangle$, contributes. We separate the contribution of $\langle \mathbf{f_G} \rangle$ from the total pressure (black asterisks), and the result is plotted as the red circles in Fig. 3.3(c). In general, the pressure is proportional to
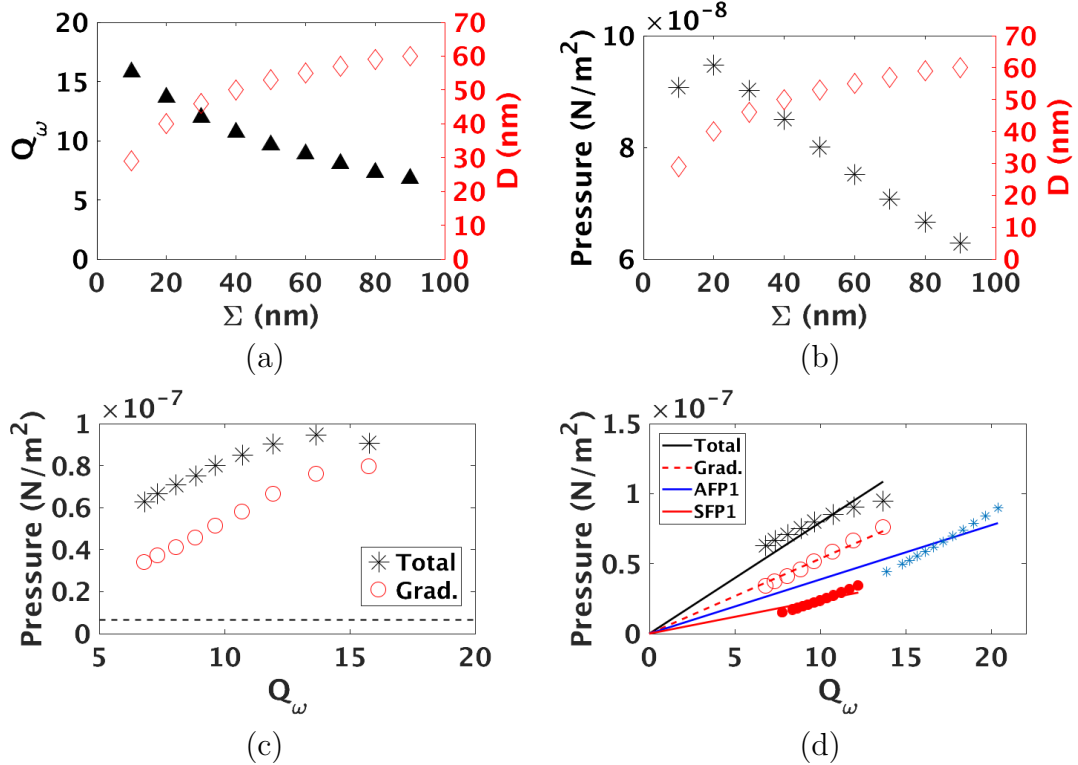
Fig. 3.3. Simulation results for the nanostructured slot cavity array in Au, and with reference to Fig. 3.1(d): $\Lambda = 400$ nm and $T = 200$ nm. (a) Q_ω (triangles) and resonant slot depth, D (diamonds), as a function of slot width, Σ. (b) Radiation pressure (asterisks) along with the resonant D (diamonds) as a function of Σ. In general, smaller Σ results in higher Q_ω and larger pressure, consistent with the asymmetric 1D Fabry-Perot cavity results of Fig. 3.2(d), AFP3. (c) Radiation pressure as a function of Q_ω, decomposed into total and gradient ($\langle \mathbf{f_G} \rangle$) contributions. The dashed line shows the maximum pressure on a perfect mirror. The nanostructured slot cavity supports a pressure enhancement more than a order of magnitude higher than a perfect mirror. (d) Radiation pressure as a function of Q_ω for the lower Q 1D cavities, from Fig. 3.2, in comparison with the slot pressures from (c). The black line and red dashed line are the linear fits to the total pressure and $\langle \mathbf{f_G} \rangle$, respectively from the first 8 points in (c). The blue and red lines are the linear fits to P_{M2} for AFP1 and SFP1, which are low-Q Fabry-Perot cavities in the examples considered, for comparison. The nanostructured slot cavity is more efficient in delivering radiation pressure enhancement on a target surface than the 1D Fabry-Perot cavity when the cavities have the same Q.

Q_ω and the relationship is linear for lower Q_ω. Higher Q_ω supports a higher pressure contribution from $\langle \mathbf{f_G} \rangle$, although the total pressure reduces at the highest Q_ω. The dashed line is again the maximum pressure on a perfect mirror, from Fig. 3.2(d). Compared to the net pressure for the 1D AFP3 in Fig. 3.2(d), the slot cavity can provide a pressure enhancement more than a order of magnitude higher than a perfect mirror with a relatively low-Q cavity. The gradient of the total pressure in Fig. 3.3(c), dP/dQ_ω, describes the efficacy of the cavity in enhancing the pressure (per unit Q or stored energy). In Fig. 3.3(d), we plot the linear fits passing through the origin for the total pressure and the pressure contributed by $\langle \mathbf{f_G} \rangle$ as black and red dashed lines, respectively, using the first 8 points (linear region) in Fig. 3.3(c). Linear fits to the pressure as a function of Q_ω for SFP1 and AFP1, which involve similar (low) Q_ω to the slot cavity, are plotted for comparison as the red and blue lines, respectively, in Fig. 3.3(d). The nanostructured slot cavity can provide larger pressure enhancement on the target surface than that (on M_2) for the 1D Fabry-Perot cavities we considered when the cavities have the same Q. This is mainly due to the contribution of the gradient force, $\langle \mathbf{f_G} \rangle$. Consequently, for a incident wave with time-averaged intensity of S, the nanostructured slot cavity can utilize the energy stored in the cavity more efficiently in creating optomechanical pressure by drawing on both $\langle \mathbf{f_R} \rangle$ and $\langle \mathbf{f_G} \rangle$.

3.4   Conclusion

We have presented the physical basis of the enhanced pressure on a nanostructured metallic surface as being due to an asymmetric Fabry-Perot resonance. This is evident from the relationship between the total pressure on an asymmetric 1D cavity to the slot array, as a function of Q. The enhanced pressure for the nanostructured metal film results from both terms in (3.1), where the cavity mode resonance influences the fields in the metal and hence the force density and pressure. Generally, increasing the cavity Q can produce higher pressure. There are convenient fabrication methods for such nanocavity arrays in metal, for example, direct nanoimprinting [75]. Resonant

cavities formed on surfaces and with other materials should also provide enhanced pressure. With use of optimized, aperiodic structures, more control and higher pressure should be possible [18], such as through use of geometry as variables and with multiple wavelengths. The explanation for enhancement we have provided allows design guidelines for applications that will benefit from enhanced and controllable optical forces with structured material. For example, beads that are used in optical tweezers could be structured [76]. More generally, we suggest that there are new opportunities related to the interaction of waves with materials and the generation of a mechanical response.

4. ELECTROMAGNETIC PRESSURE WITH BINARY APERIODIC NANOSTRUCTURES

The electromagnetic force on matter depends on both the geometry and material properties, and for a contiguous material, the pressure is a useful metric. We present a statistical method with example results that allows the evaluation of pressure in relation to a nanostructured material arrangement with unexpected conclusions. We show that it is possible to obtain a pressure substantially greater than that on a perfect, planar mirror, and relate this to resonant field features. With some material arrangements, the pressure can be negative, and this can again be related to resonances. Negative pressure can be understood as being due to the total field, a superposition of the incident and scattered fields, where the structure regulates the local scattered field and hence the pressure through an integral of the resulting force density. The statistical analysis provides physical insight into how to regulate both the pressure magnitude and direction and hence provides a framework for applications. The fields impacted include biophysics, where information is obtained about biomolecules from force and torque measurements, cavity optomechanics related to basic science and sensing, and optical remote control and actuation, where regulation of the magnitude and direction, and the possibility of materials with multiple functionalities, provides new opportunities.

4.1   Introduction

The radiation pressure on a silver mirror was measured more than one century ago [77], confirming the mechanical properties of light [54]. The prediction of force experiments is the requirement for any force theory, and there is a substantial history related to models [70, 71, 78–82]. Two important experiments were designed in

this regard [83, 84]. The 1978 Jones and Leslie mirror experiment has yielded more information to explore the dependence of the radiation pressure on a mirror and the background material [83] and the 1973 Ashkin and Dziedzic water experiment has established the initial work studying the optical force from a spatially varying electromagnetic field with polarizable media [84], which led to the invention of optical tweezers [56]. The trapping force exerted by strongly focused fields on small particles has become important in applications such as optical manipulation in biology, physical chemistry, and soft condensed matter physics [13]. Also, the influence of the environment on the local force has produced interesting force features [85–89], suggesting that the fields scattered or controlled by surfaces or material structure provides new opportunities in the control of particles.

We describe the collective force on a nanostructured material where the scattered field due to the material modifies the total field and hence the pressure. The force magnitude we find, in relation to a perfect mirror, and the direction control, present unexpected opportunities. While the optical force is related to a change in optical momentum, it is also a function of the field spatial distribution in the material. Progress in describing the optical force within homogeneous bulk materials [12], small objects [13] or periodic structures [14] has revealed some important understanding related to optical manipulation. For example, a structured gold surface can provide a large enhancement of the optical force [11], relative to a perfect mirror, due to the enhanced fields in a array of asymmetric cavities and the excitation of surface waves. This raises the question of the relationship between structured material and the resulting optical force. We consider this issue in the context of aperiodic structures that have a large number of degrees of freedom and hence offer more electromagnetic field control relative to periodic systems when implemented as waveguide [2–4, 15–17] and diffractive [5] elements. Few guidelines exist for the design of aperiodic materials [24, 25], which rely on optimization-based solutions, but insight into control of the scattered fields has been provided by a multivariate statistical analysis of binary

aperiodic structures [18]. We consider here how the large number of degrees of freedom supported by aperiodic materials contributes to the control of the optical force.

We present results for the electromagnetic pressure on binary aperiodic structures that show an ability to tune from strong pushing to strong pulling relative to that on a perfect mirror. A net pulling optical force has been identified previously for small particles trapped in beams [87,90] or gain media [65,91]. We show that negative pressure can occur in a passive material with plane wave illumination. The resonant field features within the structured material can have a significant impact on the optical force, as we describe. These results suggest new opportunities in optomechanics that draw on the structure-force relationships we identify.

We summarize the optical force density theory used in Sect. 4.2, and the integral of this force density over the material divided by the lattice dimension results in the pressure. Section 4.3 describes the specifics of the aperiodic structure investigated, and Sect. 4.4 the formation of the field correlation matrix and the statistical analysis employed. Section 4.5 describes our pressure and field covariance eigenvalue results, establishing a link and a metric between structure and force, including direction control. The resonance basis for large positive and negative pressure is established through example field and force density solutions described in Sect. 4.6. A discussion of issues and applications is presented in Sect. 4.7 and conclusions in Sect. 4.8.

4.2   Optical Pressure Theory

The force expression we utilize here, originally from Einstein and Laub [70], has been derived by Penfield and Haus [71] and investigated by others [11,12,65,66,92,93], and is given by

$$
\begin{aligned}
\mathbf{f} \;=\; & \frac{\partial \mathbf{P}}{\partial t} \times \mu_0 \mathbf{H} - \frac{\partial \mu_0 \mathbf{M}}{\partial t} \times \epsilon_0 \mathbf{E} \\
& + \rho \mathbf{E} - \mu_0 \mathbf{H} \times \mathbf{J} + (\mathbf{P} \cdot \nabla)\,\mathbf{E} + \mu_0\,(\mathbf{M} \cdot \nabla)\,\mathbf{H},
\end{aligned}
\tag{4.1}
$$

with SI units of $\mathrm{N/m^3}$, where $\mathbf{E}$ is the electric field, $\mathbf{H}$ is the magnetic field, $\mathbf{P}$ is the polarization, $\mathbf{M}$ is the magnetization, $\mathbf{J}$ is the electric current density, ρ is the electric

charge density, ϵ_0 is the permittivity of free space, and μ_0 is the permeability of free space. We assume that in the source-free case, $\mathbf{J}$ and ρ are both zero, and also that no magnetic material response exists, thus the terms including $\mathbf{M}$ can be neglected. We consider a time-harmonic, monochromatic field with time convention $\exp(-i\omega t)$ within an isotropic material, giving $\mathbf{P}\left(\mathbf{r}, \omega\right) = \epsilon_0 \chi_E\left(\mathbf{r}, \omega\right) \mathbf{E}\left(\mathbf{r}, \omega\right)$, where χ_E is the electric susceptibility. Under this assumption and with the frequency domain implied, the time average of (4.1) becomes

$$\langle \mathbf{f} \rangle = (\hat{\mathbf{e}} \times \hat{\mathbf{h}})\frac{\mu_0 \epsilon_0 \omega}{2}\Im\left\{\chi_E E(\mathbf{r})H^*(\mathbf{r})\right\} + \frac{\epsilon_0}{2}\Re\left\{(\chi_E E(\mathbf{r})\hat{\mathbf{e}} \cdot \nabla)(\hat{\mathbf{e}}E^*(\mathbf{r}))\right\}, \quad (4.2)$$

where $\hat{\mathbf{e}}$ and $\hat{\mathbf{h}}$ are unit vectors indicating the direction of the electric and magnetic field phasors E and H at position $\mathbf{r}$, respectively, $\Re\{\cdot\}$ is the real part and $\Im\{\cdot\}$ the imaginary part, and peak sinusoidal amplitudes have been assumed. We apply a frequency domain finite element method (FEM) to obtain the numerical field solutions [49]. The numerical field solution provides the scattered field, and the total field is obtained by adding the known incident field. The force densities are found using (4.2), and the pressure obtained from the normalized integral of the force density.

4.3 Aperiodic Nanostructured Material

Figure 4.1 shows the 2D geometry of the binary aperiodic nanostructured material we consider. A $\lambda_0 = 633$ nm plane wave is normally incident from the left in free space with $\mathbf{H}$ in the $\hat{\mathbf{z}}$ direction. The material structure is defined within a wavelength-sized region (633 nm on a side). This domain is divided into $P \times P$ pixels. Each pixel can be either the scatterer or the background (free space). Fixing the fill factor, f, specifies the number of scatterers. We do this by truncating the number formed from fP^2 to an integer value. To avoid singularities in the numerical simulations, the side of each scatterer is reduced by 1 nm and the corners are rounded with a radius of 1 nm. The maximum mesh element size in the scattering material is $\lambda_0/200$, adequate to support the accuracy of the force density solutions. The top and bottom of the computational domain are bounded by perfect electric conductor (PEC) surfaces to form a cavity or
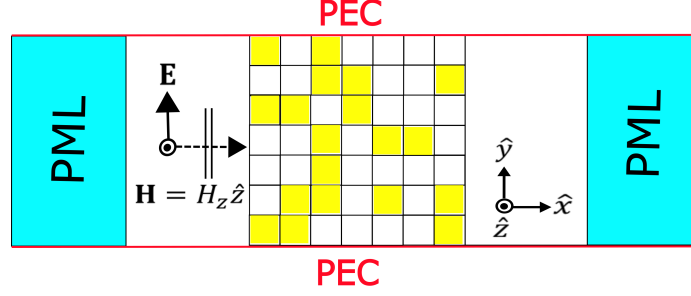
Fig. 4.1. Binary aperiodic nanostructured material simulation geometry: PML, perfectly matched layer; PEC, perfect electric conductor. A $\lambda_0 = 633$ nm plane wave with $\mathbf{H}$ in the $\hat{\mathbf{z}}$ direction is normally incident from the left. The binary nanostructured material is divided into $P \times P$ elements and each element is either the scatterer or the background (free space in our case). To avoid singularities in the numerical simulations, the side length of each scatterer is reduced by 1 nm, and the corners are rounded with a radius of 1 nm. The width and length of the discretized region is 633 nm.

a waveguide. We apply perfectly matched layers (PMLs) on both the left and right boundaries. All simulations assume an incident power density of 1 W/m^2.

The pressure is calculated from the integral of $\langle f_x \rangle = \langle \mathbf{f} \cdot \hat{\mathbf{x}} \rangle$, where $\langle \mathbf{f} \rangle$ is from (4.2) and the direction of $\hat{\mathbf{x}}$ is shown in Fig. 4.1, over all scatterers in the aperiodic nanostructure and then divided by the exposed surface (633 nm in our 2D simulations). While the segments of the aperiodic structure are not contiguous, we assume that another material can provide the structure, making the use of pressure meaningful.

4.4 Statistical Field and Pressure Analysis

We utilize a multivariate statistical method to relate field control (regulation of the scattered field, as a function of position here) and pressure control (the average force magnitude and direction) to the attributes of the binary nanostructures. Consider the transmission matrix, $\mathbf{T}$, defined as

$$\mathbf{T} = \left[\frac{H_u}{H_{iv}} \right], \quad v \in [1, ..., \Upsilon] \quad u \in [1, ..., U], \tag{4.3}$$

where H_{iv} is the incident (plane wave) magnetic field along points on the constant-x input line (with an absolute position that is unimportant) and H_u is the total field along the output line (and we choose a constant-x line that is $\lambda_0/8$ behind and to the right of the structure). The H_u samples are therefore in the near-field and influenced by both propagating and evanescent fields. In the simulations, we choose $\Upsilon = U = 101$ and divide the input and the output lines (the 633 nm long input and output lines between the two PEC surfaces in Fig. 4.1) into uniformly spaced points. The $(U \times U)$ field covariance matrix, $\mathbf{C}$, can be calculated as [94]

$$\mathbf{C} \;=\; \langle \mathbf{T}^H \mathbf{T} \rangle - \langle \mathbf{T}^H \rangle \langle \mathbf{T} \rangle, \tag{4.4}$$

where H is Hermitian transpose and $\langle \cdot \rangle$ is the average over all samples. A sample means a particular nanostructured scattering material arrangement, resulting in a specific $\mathbf{T}$.

The variance of $\mathbf{C}$ is defined as [94]

$$\sigma_C^2 = \sum_{u=1}^{U} \sigma_u^2 = \sum_{u=1}^{U} C_{uu} = \mathrm{Tr}\{\mathbf{C}\}, \tag{4.5}$$

where the C_{uu} are the diagonal elements of $\mathbf{C}$ and $\mathrm{Tr}\{\cdot\}$ is the trace. It can be shown (see, for example, [45] page 264) that

$$\mathrm{Tr}\{\mathbf{C}\} = \sum_{u=1}^{U} \lambda_u, \tag{4.6}$$

where the λ_u are the eigenvalues of $\mathbf{C}$. Therefore, from (4.5) and (4.6),

$$\sigma_C^2 = \sum_{u=1}^{U} \lambda_u, \tag{4.7}$$

which we term the variance of $\mathbf{C}$ and use to appraise field control on the transmission side.

The reflection matrix is defined by $\mathbf{R} = [H_r/H_{iv}]$, where H_r is the reflected field on the input side at $\lambda_0/8$ from the nanostructure, and the corresponding σ_C^2 can be likewise obtained. A large variance indicates that the binary arrangement has a large impact on the scattered field, thus suggesting more control efficacy or increased degrees of freedom for field control.

4.5 Pressure in Relation to Field Covariance

We first investigate the relationship between the nanostructure and both the field and force control with an example metallic material. Gold (Au) with a dielectric constant of $\epsilon = -11.75 + i1.26$ at 633 nm [95] in a free space background is assumed. Figure 4.2(a) shows results for $f = 0.2$ and Fig. 4.2(b) for $f = 0.5$. We use (4.7) to obtain σ_C^2 by randomly selecting 300 arrangements and then a resampling method [18] to obtain the mean $\langle \sigma_C^2 \rangle$ and deviation of σ_C^2. Figure 4.2 shows the statistical results for $\mathbf{T}$ (blue dashed-dotted line) and $\mathbf{R}$ (blue dotted line), along with the deviations, as a function of P. The strong scatter associated with Au scatterers provides relatively larger reflection than transmission, and thus more control on the incident side, exhibited in the larger σ_C^2 associated with reflection. Increasing f increases σ_C^2 under reflection and reduces the control for transmission. With finer discretization through an increase in P, the field control becomes weaker, indicated by a decreasing σ_C^2 in Figs. 4.2(a) and (b) for both reflection and transmission. We interpret this as being due to the onset of homogenization.

The corresponding statistical data for total pressure with nanostructured Au is shown in Fig. 4.2 as the orange solid line, along with the deviations for each P. The triangles indicate the maximum total pressure found through this procedure in the positive $\hat{\mathbf{x}}$ direction, resulting in a pushing force. We should note that these results are not the maximum possible pressures. The asterisks show the minimum (with respect to the $\hat{\mathbf{x}}$ direction) pressures found in each case, and some arrangements result in a negative pressure and hence a pulling force on the nanostructure (that can be quite large).

The maximum radiation pressure on a perfect mirror is given by $2S/c$, where S is the magnitude of the incident Poynting vector and c is the free space velocity, with the implication that this is the background medium. This result was presented by Maxwell and is widely used [54]. With the assumed $S = 1$ W/m^2, the pressure on a perfect mirror is approximately 6.67×10^{-9} N/m^2 with normal incidence. As a
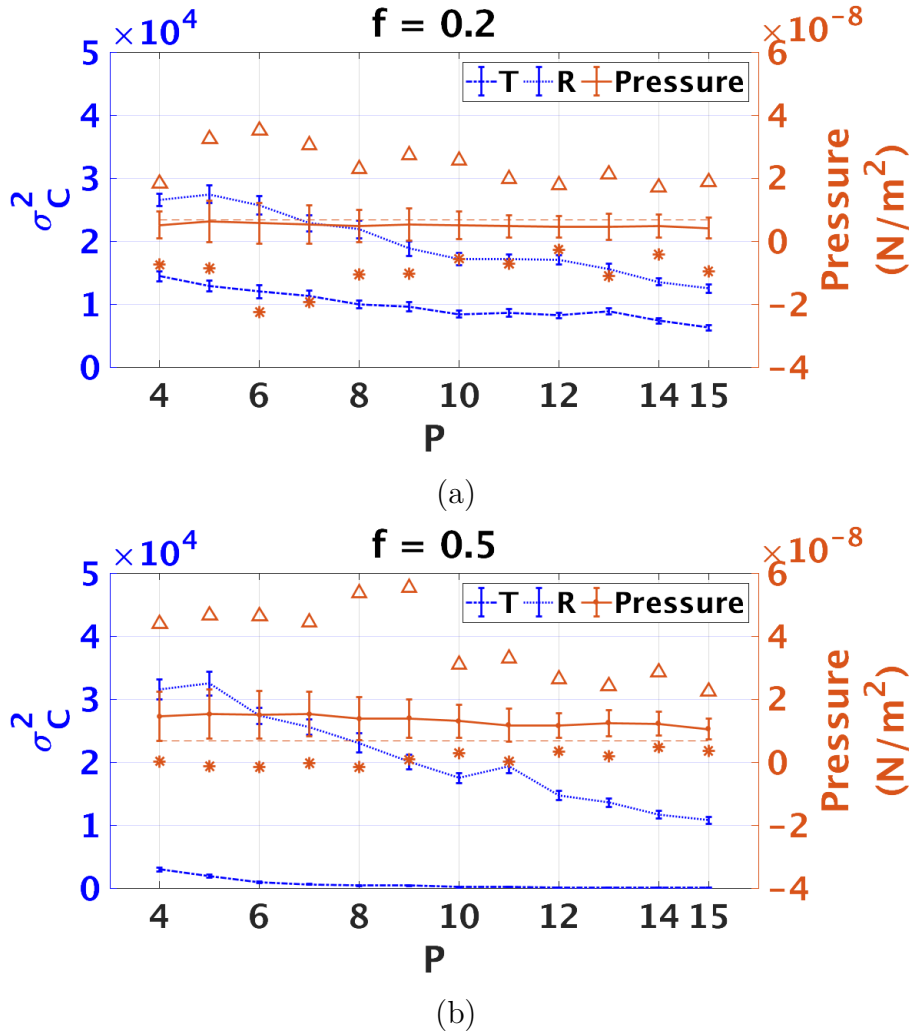
Fig. 4.2. The variance for aperiodic nanostructured Au, σ_C^2, measured $\lambda_0/8$ from the discretized domain, and the optical pressure as a function of discretization, P, with fill fraction: (a) $f = 0.2$ and (b) $f = 0.5$. Referring to Fig. 4.1, the magnitude of the normally incident power density is 1 W/m^2. The blue dotted line and blue dashed-dotted line, relate to the left axis and describe σ_C^2 from the reflection and transmission matrices, $\mathbf{R}$ and $\mathbf{T}$, respectively. The standard deviation bars were calculated from a resampling method. The orange solid line refers to the right axis and describes the corresponding radiation pressure on the binary material and the deviations from the analysis. The orange dashed line indicates the maximum pressure on a perfect mirror. The triangles and asterisks show the maximum and minimum radiation pressure, respectively, in the direction of the incident wave ($\hat{\mathbf{x}}$ direction). The pushing and pulling forces correlate with σ_C^2 from the reflection and transmission matrices $\mathbf{R}$ and $\mathbf{T}$, respectively.

reference, this perfect mirror result is plotted as the orange dashed line in Figs. 4.2(a) and (b), with the understanding that there is no relationship to P. From Fig. 4.2(a) and for $f = 0.2$, our simulations yielded a maximum positive pressure that is around 5 times larger than that on a perfect mirror. With $f = 0.5$ and from Fig. 4.2(b), the pressure enhancement can be even larger and reaches around an order of magnitude higher than that on a perfect mirror. Note also that the mean pressure for $f = 0.5$ is higher than the result for the perfect mirror. Worthy of additional comment is the unexpected result that the range of the variances of the total pressure (deviation bars for the orange lines) and the minimum pressure (asterisks) in Figs. 4.2(a) and (b) indicate that some material arrangements support the total pressures in the negative $\hat{\mathbf{x}}$ direction, namely, pulling against the direction of the incident wave. Gain [65, 91] and control over a particle with a special beam profile [87, 90] have been found to produce negative forces, but our results indicate that a structured material with a single incident plane wave can have a net negative force. This pulling force should be important in applications such as optical switching.

We observe from Fig. 4.2 that a large $\langle \sigma_C^2 \rangle$ for $\mathbf{R}$, the blue dotted line, promotes control of the pushing force, namely the deviation of the positive pressure, and that large $\langle \sigma_C^2 \rangle$ for $\mathbf{T}$, the blue dashed-dotted line, suggests control of the pulling force. As $\langle \sigma_C^2 \rangle$ reduces with increasing P in Fig. 4.2(a), the deviation and the maximum and minimum pressure also tends to reduce. This is the case for both pushing and pulling, and the relatively high σ_C^2 for $\mathbf{T}$ in this case is indicative of a capacity to enable pulling. The oscillations in the maximum and minimum pressures in Fig. 4.2(a) relate to resonances, and we will revisit this issue. While the smallest discretization level appears as an anomaly to this trend, we attribute this to insufficient statistics for that case. The relationship between σ_C^2 and pressure is further reinforced in Fig. 4.2(b), for $f = 0.5$. This large fill case results in small transmission and little field control on that side. The minimum pressures in this case are around zero, showing little control to produce a pulling force. However, σ_C^2 for $\mathbf{R}$ is high in Fig. 4.2(b), and the pressure deviations and maxima are large. As with $f = 0.2$, a decreasing $\langle \sigma_C^2 \rangle$ corresponds to

a reduction in the pressure deviation and the maxima. We conclude that the ability to control fields on the transmission side promotes a pulling force. With an incident H_z, plasmon surface waves are excited. Exciting such surface waves on the back of the aperiodic structure, on the transmission side, can lead to a pulling force. While σ_C^2 measures field control and pressure has the influence of the material properties, with a fixed fill, field control implies force control.

Now we consider aperiodic nanostructured dielectric materials. We choose silicon (Si) as the scattering material because it is important for integrated photonics and has been widely used in nano-scale fabrication. The dielectric constant assumed for Si at a wavelength of 633 nm is $15.07 + i0.15$ [96]. Figure 4.3(a) shows the near-field field variance (σ_C^2) and pressure data as a function of P, with $f = 0.2$, obtained on a line $\lambda_0/8$ in front of and behind the region discretized, and Fig. 4.3(b) presents our results for $f = 0.5$. The deviations of the total optical pressure show that the enhancement is overall larger with $f = 0.5$ than that with $f = 0.2$, because the binary nanostructure occupies a larger scattering volume. Similar to the cases for Au scatterers, both σ_C^2 and pressure deviation decrease with increasing P due to homogenization for $f = 0.2$ in Fig. 4.3(a). We do not observe this trend for $f = 0.5$ in Fig. 4.3(b), possibly because the large fill fraction has a more stringent (larger) volume requirement to reach homogenization, and the fact that Si offers prospects for high transmission and reflection at high fill. For the Si case, the deviation of the pressures is smaller than those found for Au because of the weaker scatter. However, the maximum radiation pressure can still reach around 3 times larger than that on a perfect mirror, shown again as the orange dashed lines in Fig. 4.3. Figures 4.3(a) and (b) show that Si aperiodic structures can also provide a pulling force. Both fills offer substantial negative pressures, as indicated by the asterisks. We understand this by the relatively high transmission compared to the equivalent cases for Au. The deviation and the maximum values of the pressure are larger for the higher fill case. Our results show that dielectric materials are also good candidates for optical pressure

enhancement and optomechanical applications. Both pushing and pulling pressures can be substantial greater than that on a perfect mirror.

The σ_C^2 data in Fig. 4.3 for Si again provides insight into the pressure. When $f = 1$, $\sigma_C^2 = 0$, so the increasing fill will eventually result in loss of field control and hence, presumably, reduced pressure enhancement. Resonant features can be observed in the results for $\langle \sigma_C^2 \rangle$ as a function of P, as found in earlier work [18]. The cases in Fig. 4.3(a) where the local maximum $\langle \sigma_C^2 \rangle$ from the transmission matrix $\mathbf{T}$ (for example, the blue dashed-dotted line for $P = 7$) and the local maximum $\langle \sigma_C^2 \rangle$ from the reflection matrix $\mathbf{R}$ (for example, the blue dotted line with $P = 5$) are suggestive of series-resonance (high transmission) and parallel-resonance (high reflection), respectively. Corresponding to these observations for $\langle \sigma_C^2 \rangle$, the mean pressure for $P = 5$ is larger than for $P = 7$. Consequently, given the pressure deviations for these two levels of discretization, the parallel resonance ($P = 5$) is likely to result in pushing, but the statistical data for pulling with series resonance ($P = 7$) is inconclusive for this fill. The case for $P = 5$ in Fig. 4.3(b) has large $\langle \sigma_C^2 \rangle$ for $\mathbf{R}$ and a correspondingly large mean pressure, whereas for $P = 7$, where $\langle \sigma_C^2 \rangle$ dips, there is a small mean pressure. This again suggests control of the reflected fields promotes pushing. Consider now $P = 11$, which has the largest $\langle \sigma_C^2 \rangle$ for $\mathbf{T}$ and also large $\langle \sigma_C^2 \rangle$ for $\mathbf{R}$, possibly supporting both series and parallel resonances and providing the largest pressure deviation and promoting substantial pulling. Our conclusion is that for both dielectric and metallic scatterers, σ_C^2 is a useful metric to investigate pressure.

4.6   The Influence of Field Resonances on Pushing and Pulling

The statistical results from Figs. 4.2 and 4.3 show oscillatory features as P is varied. These variations are prominent in the $\langle \sigma_C^2 \rangle$ data in Fig. 4.3, but also clearly evident in the maxima and minima of the pressures for both the Au and Si structures. This data suggests field resonances within the structures and, importantly, that these
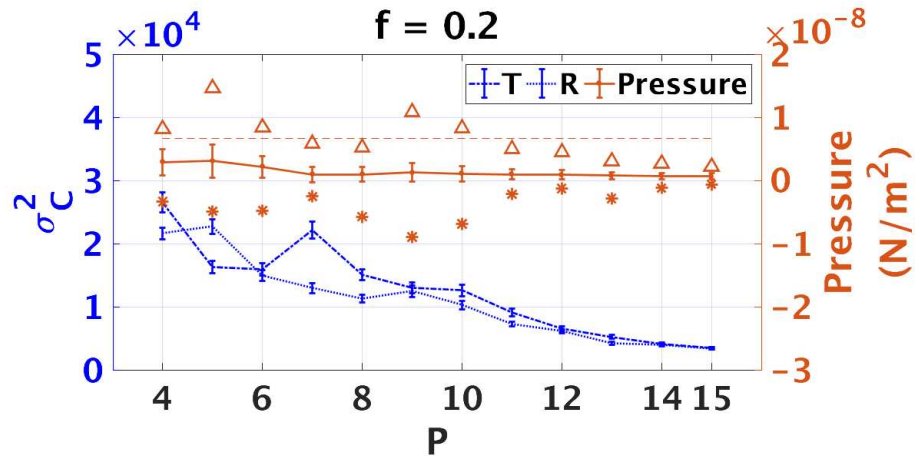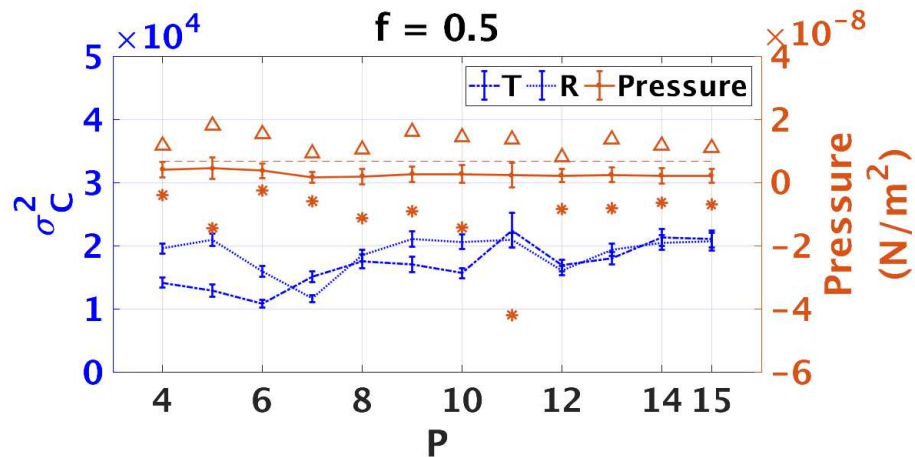
Fig. 4.3. The variance for aperiodic nanostructured Si, σ_C^2, measured $\lambda_0/8$ from the discretized domain, and the optical pressure as a function of discretization, P, with fill fraction: (a) $f = 0.2$ and (b) $f = 0.5$. The magnitude of the normally incident power density is 1 W/m^2. The blue dotted line and blue dashed-dotted line, refer to the left axis, describe σ_C^2 from $\mathbf{R}$ and $\mathbf{T}$, respectively. The standard deviation bars were calculated from the statistical analysis. The orange solid line refers to the right axis and describes the corresponding radiation pressure on the binary material, and the bars show the standard deviations in the samples. The orange dashed line indicates the max pressure on a perfect mirror. The triangles and asterisks show the maximum and minimum radiation pressure, respectively, in the $\hat{\mathbf{x}}$ direction. Aperiodic dielectric structures can also support both enhancement and the control of the direction of the optical force.

may play a role in achieving large positive or negative pressure. Here, we investigate the physical resonance effects within the binary materials by observing the field and corresponding optical force density distribution for specific material instances with maximum pushing/pulling optical force.

Consider the case for Au in Fig. 4.2(a) for $f = 0.2$ with the maximum pushing force, which occurs when $P = 6$ ($\{P, P\} = \{6, 6\}$, where the triangle indicates a pressure of about 3×10^{-8} N/m^2). Figure 4.4(a) shows the binary nanostructure arrangement for this case. The magnitude of the electric and magnetic field distributions with normal incidence is given in Figs. 4.4(b) and (c), respectively. Figure 4.4(d) shows the time-averaged optical force density, $\langle f_x \rangle = \langle \mathbf{f} \cdot \hat{\mathbf{x}} \rangle$, from (4.2). The magnitude of the electric field and the force density distributions are normalized to 1 V/m and 1 N/m^3, respectively, and presented on a log scale (dB) in order to distinguish the large contrast in the local values. The relatively large reflected fields can be observed in both Figs. 4.4(b) and (c), and there is evidence of plasmon surface waves that have a substantial influence on the force density in Fig. 4.4(d). Notice that significant reflection and control over the reflected fields, as measured by σ_C^2 in Fig. 4.2(a), promotes a large pushing force. In an equivalent circuit sense, this corresponds to a parallel resonance, thereby inducing a large reflection.

Next, we consider the case of Au with the same resolution, $P = 6$, but supporting the maximum pulling force (the asterisk in Fig. 4.2(a)). The arrangement of Au scatterers for this example is shown in Fig. 4.5(a). We plot the magnitude of the electric and magnetic field distributions in Figs. 4.5(b) and (c), respectively. Figure 4.5(d) shows the force density $\langle f_x \rangle$. A larger proportion of negative (in the $-\hat{\mathbf{x}}$ direction, namely, pulling) force density can be found within each scattering element, and this results in the cumulative negative pressure. Different from the field distributions in Fig. 4.4 for the pushing case, the larger fields on the transmission side can be observed in Figs. 4.5(b) and (c), consistent with a series resonance. Note the surface wave excited on the right-hand side of the structure that is very evident in the magnetic field

$20 \log_{10}|\mathbf{E}|$ (dB)

(a)   (b)

$|\mathbf{H}|$ (A/m) $10 \log_{10}<f_x>$ (dB)

(c)   (d)
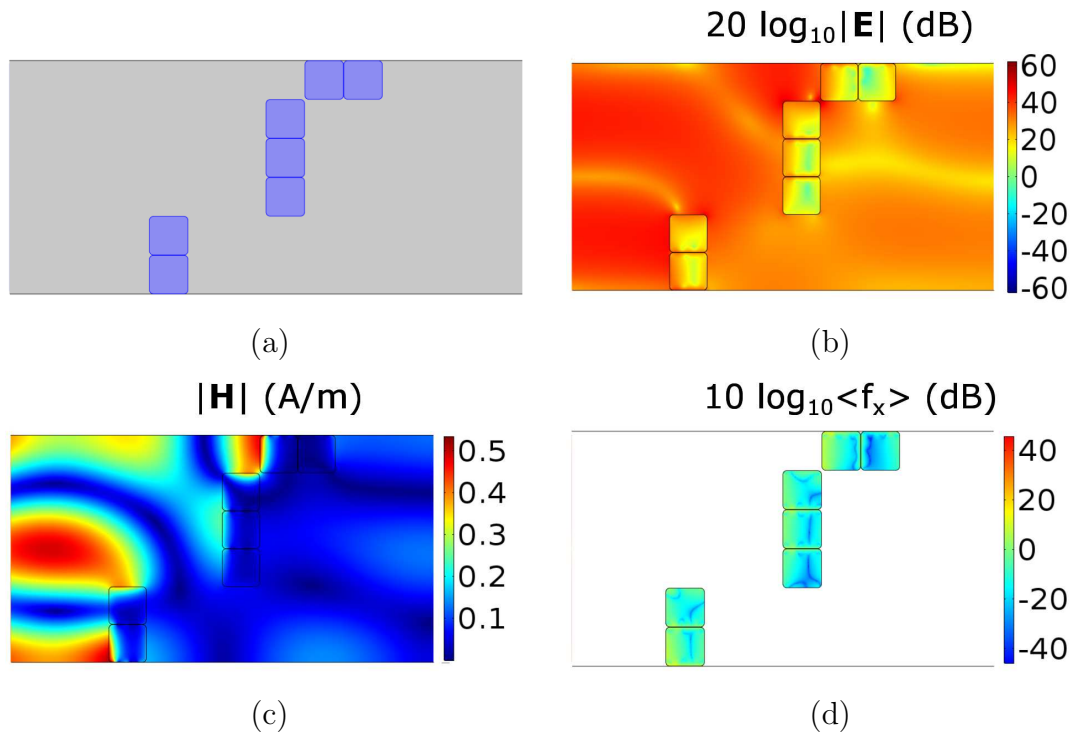
Fig. 4.4. The fields and force density for the arrangement in Fig. 4.2(a) for Au with the largest pushing force: $\{P, P\} = \{6, 6\}$ and $f = 0.2$. (a) The purple squares indicate the positions of the scatterers. (b) The electric field magnitude, normalized to 1 V/m on a log scale (dB). (c) The magnetic field distribution. (d) The time-averaged optical force density, $\langle f_x \rangle = \langle \mathbf{f} \cdot \hat{\mathbf{x}} \rangle$, normalized to 1 N/m^3 on a log scale (dB). The parallel-resonant condition in this example supports the enhanced pushing pressure.

$20 \log_{10}|\mathbf{E}|$ (dB)

(a)

(b)

$|\mathbf{H}|$ (A/m)

$10 \log_{10}<f_x>$ (dB)

(c)

(d)
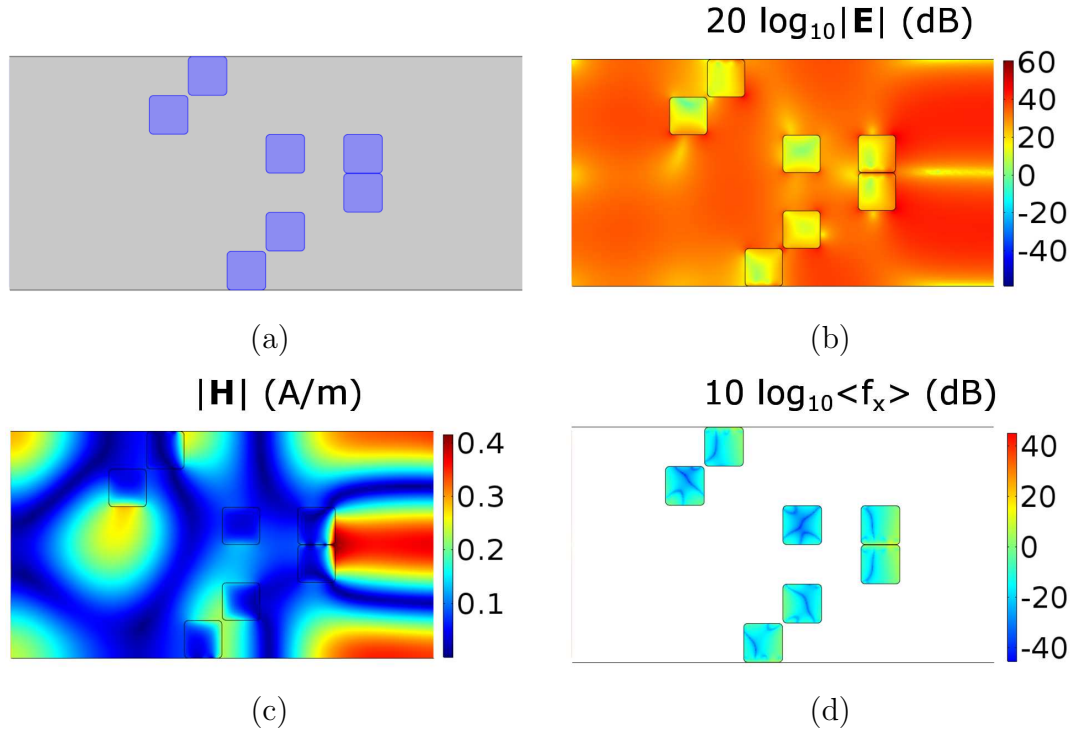
Fig. 4.5. The fields and force density for the arrangement in Fig. 4.2(a) for Au with the largest pulling force: $\{P, P\} = \{6, 6\}$ and $f = 0.2$. (a) The purple squares indicate the positions of the scatterers. (b) The electric field magnitude, normalized to 1 V/m on a log scale (dB). (c) The magnetic field distribution. (d) The time-averaged optical force density, $\langle f_x \rangle$, normalized to 1 N/m^3 on a log scale (dB). A pulling force on the scattering material is induced when the series-resonant condition occurs.

plot of Fig. 4.5(c). Excitation of a surface wave on the back can lead to a pulling force.

The fields in Fig. 4.4 for a pushing case and Fig. 4.5 for a pulling situation are consistent with the statistical results we found for σ_C^2 in Fig 4.2(a). A large σ_C^2 for reflection, as for $f = 0.2$ in Fig. 4.2(a), implies a larger maximum pushing force. Conversely, the large σ_C^2 for transmission for $f = 0.2$ in Fig. 4.2(a) results in a larger pulling force. This reveals that the fields excited by the arrangement in front of or behind the binary nanostructure relates to whether the whole geometry is pushed or pulled and to the pressure enhancement.

We observe that the arrangement of binary elements within the nanostructure plays an important role on determining the direction and enhancement of the optical force. In Fig. 4.4, when the scattering elements pack together to form a strip, the arrangement is effectively a slab of a particular length. The resulting surfaces can produce plasmon mode resonances. Those transverse resonances are most pronounced in Fig. 4.4(c), adjacent to the PEC walls at the top and bottom, and the surface wavelength in relation to the element size can be understood with use of symmetry from the boundary (the PEC is an even boundary for H_z). In the metallic case, certain arrangements can lead to very large surface fields, and hence to substantial enhancement in the pressure.

Figures 4.6 and 4.7 show the fields and force densities for maximum pushing and pulling situations with Si scatterers. Figure 4.6 is for $f = 0.5$ and $P = 5$ and the largest pushing force, where there is a σ_C^2 peak for reflection in Fig. 4.3(b). Note again the substantial amplitude of the reflected fields. However, while the metal cases supported surface waves, here the fields are confined within the dielectric. The element size in Fig. 4.6(a) is more than $\lambda_0/(2\sqrt{\epsilon})$ and hence can support a resonant mode. Local resonances are evident in the magnetic field magnitude in Fig. 4.6(c). Figure 4.7 is for $f = 0.5$ and $P = 11$, the largest pulling force case in Fig. 4.3(b). Note the large field resonances that span two or more adjacent scatterers, and the large transmitted field. As with the Au scatterer case, there is a consistent picture of large σ_C^2 for the reflected field implying a large pushing force and large σ_C^2 for transmission indicating opportunities for pulling.

4.7   Discussion and Applications

Our approach of investigating the statistical fields and pressures in binary aperiodic metal and dielectric structures sought to uncover the relationship between structure and force for basic understanding and to guide a design process in applications. We used σ_C^2 to measure field control and related this to pressure control.

$$20 \log_{10}|\mathbf{E}| \ (\text{dB})$$

(a) (b)

$$|\mathbf{H}| \ (\text{A/m})$$

$$10 \log_{10}<f_x> \ (\text{dB})$$

(c) (d)
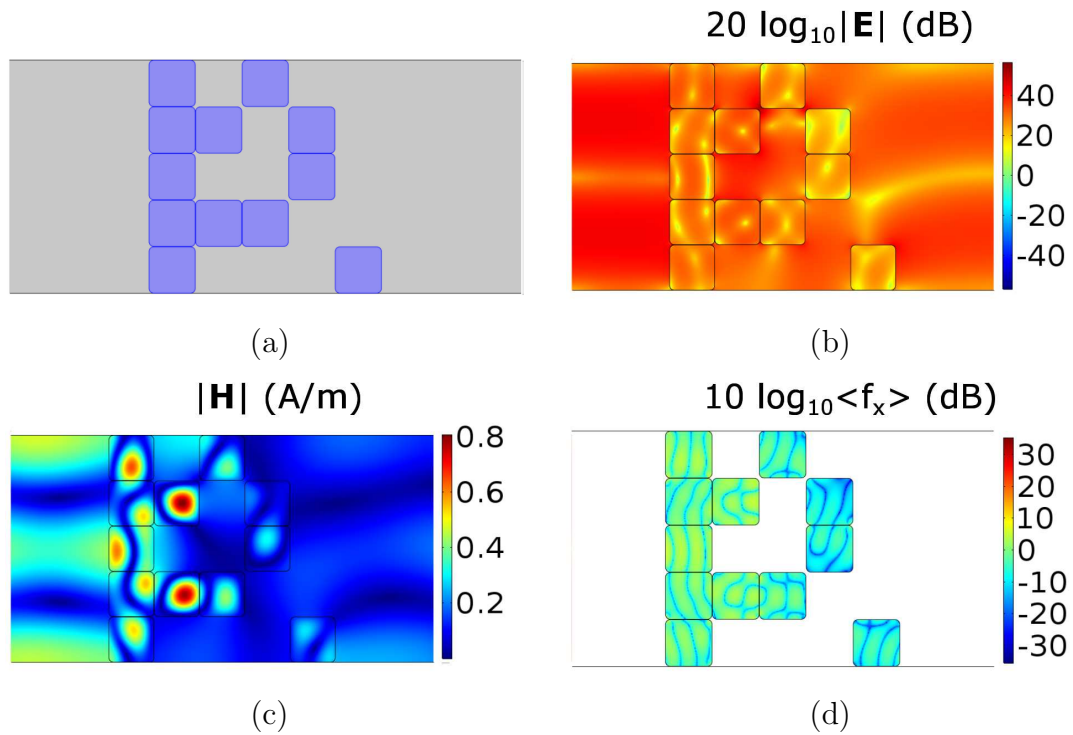
Fig. 4.6. (a) Referring to Fig. 4.3(b) for Si, the aperiodic binary nanostructure with $\{P, P\} = \{5, 5\}$, $f = 0.5$ that produced the maximum pushing force from the samples studied. The purple squares indicate the positions of the scatterers. (b) The electric field distribution, normalized to 1 V/m on a log scale (dB). (c) The magnetic field distribution. (d) The time-averaged optical force density $\langle f_x \rangle$, normalized to 1 N/m^3 on a log scale (dB). The Si pillars that form cavities in this example support the pushing pressure enhancement.
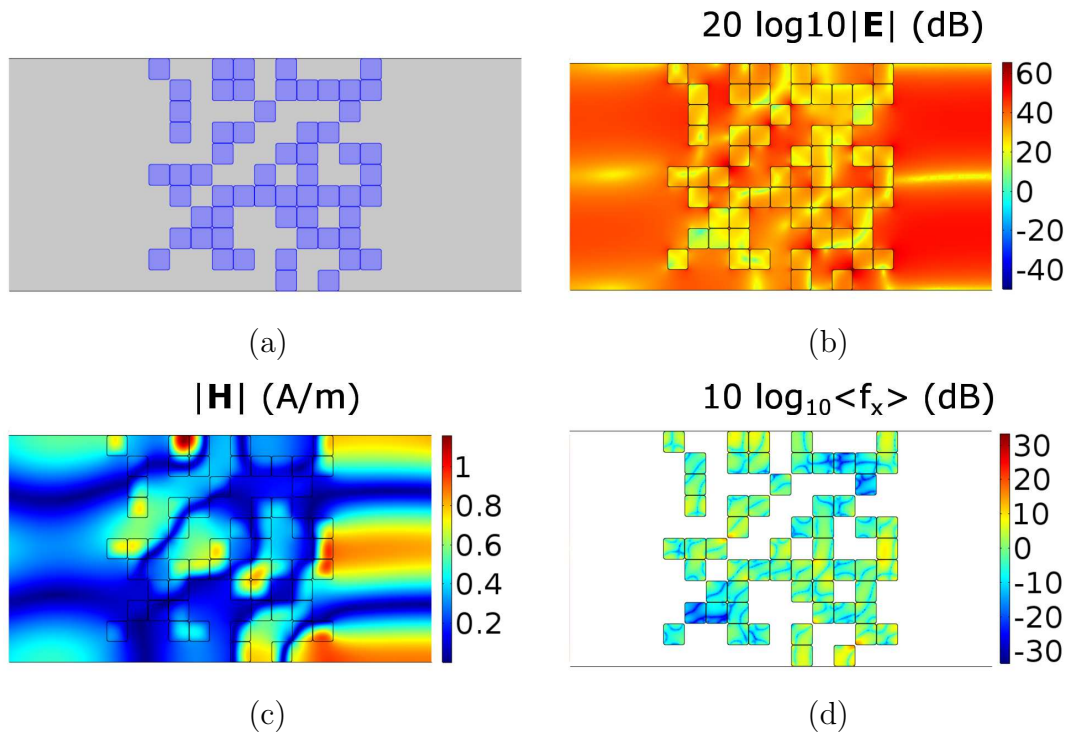
Fig. 4.7. (a) Referring to Fig. 4.3(b) for Si, the aperiodic binary nanostructure with $\{P, P\} = \{11, 11\}$, $f = 0.5$ giving the maximum pulling force in the samples over the scatterers. The purple squares indicate the positions of the scatterers; (b) The electric field distribution, normalized to 1 V/m on a log scale (dB). (c) The magnetic field distribution. (d) The time-averaged optical force density $\langle f_x \rangle$, normalized to 1 N/m^3 on a log scale (dB). The pulling force on the scattering materials is induced when the fields percolate through the Si scatterers and allow excitation on the back.

Because of the 2D analysis, it was clear that magnetic field should be used in this statistical field analysis. However, we should note that the electric field information that is relevant in the force density of (4.2) is then indirectly measured.

In measuring the mechanical response in terms of pressure, we have assumed two aspects related to the structure. First, in integrating the force density to form pressure, there needs to be a fixed relationship between segments of the aperiodic structure. Clearly, from Figs. 4.4(a), 4.5(a), 4.6(a), and 4.7(a), there are disparate regions of the scatterers. Also, we have reduced the size of the scatterers to be slightly less than the cell for numerical convenience, so even adjacently populated cells are not strictly connected. We have therefore assumed a rigid connection between the elements, as in a scaffold. This could be achieved with a background material, or in a 3D system using, for example, Si elements on SiO_2, as in a silicon-on-insulator (SOI) waveguide where Si posts are formed as the scattering elements [17]. We have assumed bulk material properties, so the small separation between cells can be neglected in a practical sense. Second, we have formed the average force expressed as a pressure over the waveguide (periodic) geometry of Fig. 4.1. This is meaningful for a physical structure composed of many periods, so that the influence of the truncation can be ignored.

The statistical pressure study we presented provides a way to explore the parameter space for a binary structure class with a large number of variables. Consequently, one can determine possible pressure enhancement opportunities and also obtain a guide for the design process with constraints. For example, we have learned that with a given fill fraction, Au provides a larger pushing force enhancement than Si. Also, a lower fill fraction promotes pulling for Au, but for Si, the high fill facilitated pulling.

The use of σ_C^2 for the reflected or transmitted fields provides a relevant measure. However, this may not be available in a design situation. Our formation of a link between fields and field correlations and the force density and pressure is intended to provide fundamental insight. This could be used in a discrete optimization design

approach [5] to reduce the computational burden. For instance, this might guide the material choice, discretization level, and spatial support. Beyond binary materials, mixture theory provides a way to tune the dielectric constants, and the boundaries could be adjusted, both as part of a continuous optimization process [4, 16]. The binary picture is then a coarse discretization in both space and material.

The fact that we found a pushing pressure greater than that on a perfect mirror warrants comment. The mirror radiation pressure has been presented as $P = 2\hbar k I$, with each photon carrying a momentum $\hbar k$ and I being the optical intensity measured in photons/$(\text{m}^2 \cdot \text{s})$, given P in N/m^2, and the factor of two is from the assumption of perfect reflection [64]. This is entirely consistent in the appropriate limit with the classical picture from Maxwell [54], where $P = S(1+|\Gamma|^2)/c$, with Γ the field reflection coefficient. Clearly, increasing I or the incident Poynting vector by increasing the quality factor in a cavity will increase the pressure on the mirrors. However, $|\Gamma| = 1$ leads to a maximum value of $P = 2S/c$. Our results show that for both Au (Fig. 4.2) and Si (Fig. 4.3) the largest pressures found were more than three times $2S/c$. This occurs because of local resonant modes within the material, allowing the net pressure to substantially exceed $2S/c$. The arrangement of Au scatterers within the PEC-bounded waveguide of Fig. 4.1 can be understood as an asymmetric cavity that can provide pressure enhancement, as in the periodic slot cavity array on a gold surface [11] but with more degrees of freedom in the geometry. This observation should be of substantial importance in applications that benefit from an increase in the relatively weak optical force. While a higher-order mode is clearly excited scattered fields, mode control could be another design dimension that would in principle allow regulation of the scattered waveguide modes (and a smaller waveguide would simply prevent the higher-order modes from propagating).

The fact that an incident plane wave can produce a pulling force may be unexpected, given earlier work where a pulling force on a bead was achieved with structure in the incident field [90]. As we have explained in relation to Figs. 4.5 and 4.7, pulling occurred with large transmission through the structure. This was facilitated by Au

with small fill or use of Si. Establishing fields on the back of the structure appears to facilitate pulling. We suggested this was established along the lines of a series resonance, in the equivalent circuit sense. However, more generally, we understand this effect as one of modifying the scattered field in a way that when superimposed with the incident field, the total field produces a force density such that pulling occurs. We should also note that this pulling force can be substantially larger than $2S/c$, based on the results we presented. A negative pressure should be important in remote control applications because a surface could be both pushed and pulled. While we have not established that this is possible in a given material, we anticipate that this could be achieved by using two different wavelengths for the incident light and designing the structure accordingly to support spectrally controlled motion.

We have associated pushing with parallel resonance (large field variance for reflection) and pulling with series resonance (small field variance for reflection). The earlier presentation of enhanced pressure based on resonance of a metal-insulator-metal waveguide mode [51] found maximum positive pressure at resonance [11], which in that case corresponded to a minimum in the far-field reflection. That situation can be viewed as a series resonance, but the transmission is small because of the thick Au, so the fields can be accumulated in front of the Au surface. Use of thinner Au and multiple layers with slots allows a regime approaching that which we considered here, and where there could be substantial fields and hence surface waves on the back.

The high transmission when there are effectively cascaded elements, as in Fig. 4.5 for Au, implies that optical percolation has occurred. A large total field therefore accumulates on the right side of the binary material system, potentially resulting in a pulling optical force (opposite to the direction of the incident light). There is therefore in principle a link between pressure and percolation theory [97, 98].

Various applications may benefit from the study we have presented. Biomolecules have been attached to beads to impart a force using optical tweezers, and this provides useful biophysical information [76]. By structuring the bead, a larger force could be imparted, and this would mean a reduction in the required laser power. It may also

be useful to have a large, structured material that provides a pushing or a pulling force in such experiments. Light sails have been used with solar propulsion. However, with structured material, a laser of the appropriate wavelength could be used. It may also be useful to use incoherent solar radiation for propulsion with aperiodic structured material, but the tradeoff between wavelength diversity and the exploitation of resonance effects to enhance the force needs to be investigated. The propulsion force (magnitude and direction) could in principle be regulated, allowing control over the trajectory of the vehicle. The deflection of an optical beam is important in displays and communication. With both pushing and pulling, a more versatile control element would be possible. It should also be expected that the principle of structured material for the control of optical forces will translate to integrated photonics. All-optical communication, rather than electronic control of photonic networks, has the promise of a substantial reduction in energy consumption [99, 100]. The use of dielectric nanostructured materials should benefit optical communication in Si-based technology. In this approach, the force imparted due to light would lead to switching, and pushing/pulling manipulation could be utilized. Our results motivate the further development of fabrication technology for aperiodic structures in optomechanical applications. Earlier work has presented ways to fabricate aperiodic waveguides [4], and an on-chip platform for controlling light-matter interactions in turbid media [101]. For example, direct nanoimprinting into metal can be used to realize nanophotonic elements [75], and that method could be used to fabricate surface-based aperiodic elements, possibly in a planarized layered arrangement.

4.8   Conclusion

We have shown that aperiodic binary nanostructures can provide a substantial enhancement in the optical pressure over that with a planar mirror, and provided insight into the basis of the effect. This enhancement is due to local resonances in the nanostructured material, as revealed by the statistical treatment and investigation of

the fields for instances of large positive and negative pressures. Perhaps unexpected is that the force imparted on a structured material by an incident plane wave can be both large and negative, and this is understood based on the scattered field due to the structured material. Previously, pulling has been presented on a small particle with a structured incident beam, and on material having optical gain. With metallic material and excitation of the surface plasmon, large pushing and pulling forces are possible. However, only slightly less than for Au in the statistical results we presented were the positive and negative pressures for Si. This is promising because of the application potential in Si photonics and because all-dielectric structured material could be more desirable in some applications. For instance, when controlling a high power laser, a large dielectric constant and low loss, with sub-bandgap light, might be desirable. Beyond physical insight into the relationship between structured material and optical forces, our results provide a constraint and a design framework.

5. CONCLUSION

In Chap. 2, we presented a multivariate statistical analysis of binary aperiodic scattering elements that provides a physical understanding of the relationship between structure and field control, from the near-field through the far-field. The eigen-decomposition of the field covariance matrix gives us a measurable number to compare the variances of fields (σ_C^2) that nanostructures can support in different cases. This allows evaluation of the degrees of freedom available for controlling the near-field through to the far-field response that can be incorporated into a design process. In addition, the field statistics also reveal dependency with the possible field control. The weakly and strongly scattering aperiodic element fields were found to be well described by circular Bessel statistics, and intermediate scattering strength resulted in Gaussian fields. With the geometry and polarization considered, the regime where zero-mean circular Gaussian field statistics hold appears to be the domain where there is more field control (and more independent phasors), and presumably where this class of aperiodic elements is optimal. The results we have presented in Chap. 2 provide design guidelines to optimize different parameters within bounded ranges, of benefit in applications.

Due to the advance of nanotechnology, nanostructured cavity extends the applications of radiation pressure enhancement from the evanescent fields and the gradient force. Plasmonic nanocavity arrays can be built using nanoimpriting [75]. This work motivates the utilization of nanostructured slot arrays for enhancing radiation pressure [11]. While other research has been focused on the interaction of a nanoparticle with the environment in a cavity or waveguide based on the concept of optical tweezer [56], the unintuitive radiation pressure enhancement on a structured surface with a value more than a order higher than a planar surface becomes possible. In Chap. 3, we presented the physical basis of the enhanced radiation pressure on a

nanostructured metallic surface as being due to an asymmetric Fabry-Perot resonance. By the use of asymmetric cavity, radiation pressure enhancement on both mirrors or on the target surface was attributed to the increase of Q or the stored energy within a cavity. In addition, the optical force in the nanostructured slot cavity involving the gradient force can be substantially increased resulting in a much stronger enhancement per unit energy than the conventional Fabry-Perot cavity. This will allow the relatively weak optical force to be significant and effective in control and propulsion applications.

In Chap. 4, we showed that aperiodic binary nanostructures can provide large field control, resulting in great enhancement in optical manipulation. A pulling optical force was found. This was previously found for small objects or slabs with the use of metamaterial. This pulling pressure becomes possible within aperiodic nanostructured slabs when the passive scattering material is metallic (Au) or dielectric (Si). The statistical results show that the resonant features from the studies of the field variance can contribute to a larger enhancement in optical force with the parameter space considered. The field and force density distribution reveal the physical mechanism of optical force manipulation as being due to the positions of the excited modes. When a metallic material is used, the surface plasmon can be excited to generate more fields accumulated assisting the enhancement of the optical force. In addition, with use of dielectric scattering material, pressure can also be controlled on both the enhancement and direction with aperiodic nanostructures. Along with motivating a fabrication technology for aperiodic nanostructures [101], our work can greatly facilitate the design process when the optimization is applied.

Based on the understanding and experiences presented in this thesis, some future directions are motivated, as follows.

1. **Optical force with localized fields:** Anderson localization occurs when the scattering is strong and a reduction in the number of contributing phasors. The field density function has been found to be a zero-mean circular Bessel distribution [8,9]. While the scattering information within the aperiodic material can

be described by the field statistics, the possible field and optical force control with localized fields with aperiodic materials could be explored to investigate new ways and unintuitive functions in optical manipulation.

2. **Limitation of the pressure enhancement on an asymmetric cavity:** In Chap. 3, we have presented the origin of the enhanced pressure as being due to an asymmetric cavity resonance. For a 2D nanostructured slot cavity array on a gold film, the enhanced pressure can reach more than an order of magnitude larger than that on a perfect mirror. While we have shown that this enhancement exists in 1D and 2D asymmetric cavities, the upper limit of the enhancement from this mechanism remains unexplored. With increasing cavity Q, a 1D Fabry-Perot cavity is expected to behave more like a symmetric cavity when both mirrors are highly reflective. This may present a well-defined limit in the 1D case.

3. **Improved optical sail:** Interstellar travel has been proposed by the use of an ultralight spacecraft with a light sail that can be propelled by a high-powered laser and accelerated to $0.2c$ [102]. However, the requirement of the design is challenging. Based on the physical understanding of the enhanced optical force presented in Chap. 2 and with optimized design using aperiodic structures, the criteria for the light sail design could be eased by more than a order of magnitude in size of the sail or in acceleration time.

4. **All-optical switching:** An on-chip platform for controlling light-matter interactions has been demonstrated with 2D disordered waveguide [101]. Effective switching in an all-optical communication network could be possible by the use of the dielectric (Si) nanostructured materials. In this approach, light would perform the switching by using the pushing and pulling optical manipulation described in Chap. 4. This design could be wavelength-based and used in a new free-space or waveguide-based all-optical switching and routing technology.

REFERENCES

REFERENCES

[1] S. M. Popoff, G. Lerosey, R. Carminati, M. Fink, A. C. Boccara, and S. Gigan, "Measuring the transmission matrix in optics: an approach to the study and control of light propagation in disordered media," *Phys. Rev. Lett.*, vol. 104, no. 10, p. 100601, 2010.

[2] T. Ul Haq, K. J. Webb, and N. C. Gallagher, "Scattering optimization method for the design of compact mode converters for waveguides," *IEEE Trans. Microw. Theory Techn.*, vol. 43, no. 3, pp. 559–565, 1995.

[3] M.-C. Yang, J.-H. Li, and K. J. Webb, "Functional waveguide mode transformers," *IEEE Trans. Microw. Theory Techn.*, vol. 52, no. 1, pp. 161–169, 2004.

[4] M.-C. Yang, H. Chen, K. J. Webb, S. Minin, S. L. Chuang, and G. R. Cueva, "Demonstration of mode conversion in an irregular waveguide," *Opt. Lett.*, vol. 31, no. 3, pp. 383–385, 2006.

[5] J.-H. Li, K. J. Webb, G. J. Burke, D. A. White, and C. A. Thompson, "Design of near-field irregular diffractive optical elements by use of a multiresolution direct binary search method," *Opt. Lett.*, vol. 31, no. 9, pp. 1181–1183, 2006.

[6] D. A. B. Miller, "Fundamental limit for optical components," *J. Opt. Soc. Am. B*, vol. 24, no. 10, pp. A1–A18, 2007.

[7] T. D. Gerke and R. Piestun, "Aperiodic volume optics," *Nat. Photonics*, vol. 4, no. 3, pp. 188–193, 2010.

[8] Y. Chen, J. A. Newman, and K. J. Webb, "Circular bessel statistics: derivation and application to wave propagation in random media," *J. Opt. Soc. Am. A*, vol. 31, no. 12, pp. 2744–2752, 2014.

[9] J. A. Newman, Y. Chen, and K. J. Webb, "Zero-mean circular bessel statistics and anderson localization," *Phys. Rev. E*, vol. 90, no. 2, p. 022119, 2014.

[10] M. L. Povinelli, S. G. Johnson, M. Lončar, M. Ibanescu, E. J. Smythe, F. Capasso, and J. D. Joannopoulos, "High-q enhancement of attractive and repulsive optical forces between coupled whispering-gallery-mode resonators," *Opt. Express*, vol. 13, no. 20, pp. 8286–8295, 2005.

[11] A. H. Velzen and K. J. Webb, "Electromagnetic force on structured metallic surfaces," *Phys. Rev. B*, vol. 92, no. 11, p. 115416, 2015.

[12] K. J. Webb and Shivanand, "Electromagnetic plane-wave forces on homogeneous material," *J. Opt. Soc. Am. B*, vol. 29, no. 8, pp. 1904–1910, 2012.

[13] D. G. Grier, "A revolution in optical manipulation," *Nature*, vol. 424, pp. 810–816, 2003.

[14] A. S. Ang, S. V. Sukhov, A. Dogariu, and A. S. Shalin, "Scattering forces within a left-handed photonic crystal," *Sci. Rep.*, vol. 7, 2017.

[15] T. Ul Haq, K. J. Webb, and N. C. Gallagher, "Optimized irregular structures for spatial-and temporal-field transformation," *IEEE Trans. Microw. Theory Techn.*, vol. 46, pp. 1856–1867, 1998.

[16] M.-C. Yang, J.-H. Li, and K. J. Webb, "Functional field transformation with irregular waveguide structures," *Appl. Phys. Lett.*, vol. 83, no. 14, pp. 2736–2738, 2003.

[17] H.-T. Chen and K. J. Webb, "Silicon-on-insulator irregular waveguide mode converters," *Opt. Lett.*, vol. 31, no. 14, pp. 2145–2147, 2006.

[18] Y.-C. Hsueh and K. J. Webb, "Electromagnetic field control with binary aperiodic nanostructures," *J. Opt. Soc. Am. B*, vol. 34, no. 10, pp. 2059–2071, 2017.

[19] E. Yablonovitch, "Inhibited spontaneous emission in solid-state physics and electronics," *Phys. Rev. Lett.*, vol. 58, no. 20, p. 2059, 1987.

[20] S. John, "Strong localization of photons in certain disordered dielectric superlattices," *Phys. Rev. Lett.*, vol. 58, no. 23, p. 2486, 1987.

[21] D. Shechtman, I. Blech, D. Gratias, and J. W. Cahn, "Metallic phase with long-range orientational order and no translational symmetry," *Phys. Rev. Lett.*, vol. 53, no. 20, p. 1951, 1984.

[22] D. A. B. Miller, "Communicating with waves between volumes: evaluating orthogonal spatial channels and limits on coupling strengths," *Appl. Opt.*, vol. 39, no. 11, pp. 1681–1699, 2000.

[23] R. Piestun and D. A. B. Miller, "Electromagnetic degrees of freedom of an optical system," *J. Opt. Soc. Am. A*, vol. 17, no. 5, pp. 892–902, 2000.

[24] D. A. B. Miller, "Fundamental limit to linear one-dimensional slow light structures," *Phys. Rev. Lett.*, vol. 99, no. 20, p. 203903, 2007.

[25] R. Piestun and C. M. de Sterke, "Fundamental limit for two-dimensional passive devices," *Opt. Lett.*, vol. 34, no. 6, pp. 779–781, 2009.

[26] C. W. J. Beenakker, "Random-matrix theory of quantum transport," *Rev. Mod. Phys.*, vol. 69, no. 3, p. 731, 1997.

[27] I. M. Vellekoop and A. P. Mosk, "Universal optimal transmission of light through disordered materials," *Phys. Rev. Lett.*, vol. 101, no. 12, p. 120601, 2008.

[28] T. W. Kohlgraf-Owens and A. Dogariu, "Transmission matrices of random media: means for spectral polarimetric measurements," *Opt. Lett.*, vol. 35, no. 13, pp. 2236–2238, 2010.

[29] O. Katz, E. Small, Y. Bromberg, and Y. Silberberg, "Focusing and compression of ultrashort pulses through scattering media," *Nat. Photonics*, vol. 5, no. 6, pp. 372–377, 2011.

[30] S. M. Popoff, A. Goetschy, S. F. Liew, A. D. Stone, and H. Cao, "Coherent control of total transmission of light through disordered media," *Phys. Rev. Lett.*, vol. 112, no. 13, p. 133903, 2014.

[31] S. F. Liew, S. M. Popoff, A. P. Mosk, W. L. Vos, and H. Cao, "Transmission channels for light in absorbing random media: from diffusive to ballistic-like transport," *Phys. Rev. B*, vol. 89, no. 22, p. 224202, 2014.

[32] M. Davy, Z. Shi, and A. Z. Genack, "Focusing through random media: Eigen-channel participation number and intensity correlation," *Phys. Rev. B*, vol. 85, no. 3, p. 035105, 2012.

[33] X. Cheng and A. Z. Genack, "Focusing and energy deposition inside random media," *Opt. Lett.*, vol. 39, no. 21, pp. 6324–6327, 2014.

[34] P. W. Brouwer, "Transmission through a many-channel random waveguide with absorption," *Phys. Rev. B*, vol. 57, no. 17, p. 10526, 1998.

[35] N. A. Bruce and J. T. Chalker, "Multiple scattering in the presence of absorption: a theoretical treatment for quasi one-dimensional systems," *J. Phys. A*, vol. 29, no. 14, p. 3761, 1996.

[36] C. W. J. Beenakker, J. C. J. Paasschens, and P. W. Brouwer, "Probability of reflection by a random laser," *Phys. Rev. Lett.*, vol. 76, no. 8, p. 1368, 1996.

[37] A. Goetschy and A. D. Stone, "Filtering random matrices: The effect of incomplete channel control in multiple scattering," *Phys. Rev. Lett.*, vol. 111, no. 6, p. 063901, 2013.

[38] A. Yamilov, S. Petrenko, R. Sarma, and H. Cao, "Shape dependence of transmission, reflection, and absorption eigenvalue densities in disordered waveguides with dissipation," *Phys. Rev. B*, vol. 93, no. 10, p. 100201, 2016.

[39] A. A. Chabanov, M. Stoytchev, and A. Z. Genack, "Statistical signatures of photon localization," *Nature*, vol. 404, no. 6780, pp. 850–853, 2000.

[40] J. Wang and A. Z. Genack, "Transport through modes in random media," *Nature*, vol. 471, no. 7338, pp. 345–348, 2011.

[41] Z. Shi and A. Z. Genack, "Transmission eigenvalues and the bare conductance in the crossover to anderson localization," *Phys. Rev. Lett.*, vol. 108, no. 4, p. 043901, 2012.

[42] M. Born and E. Wolf, *Principles of Optics: Electromagnetic Theory of Propagation, Interference and Diffraction of Light.* Cambridge university press, 1999.

[43] K. Pearson, "On lines and planes of closest fit to systems of points in space," *Lond. Edinb. Dubl. Phil. Mag.*, vol. 2, no. 11, pp. 559–572, 1901.

[44] H. Hotelling, "Analysis of a complex of statistical variables into principal components." *J. Educ. Psychol.*, vol. 24, no. 6, p. 417, 1933.

[45] B. Noble and J. W. Daniel, Eds., *Applied Linear Algebra.* Englewood Cliffs, New Jersey: Prentice Hall, 1977.

[46] B. Efron, *The Jackknife, the Bootstrap and Other Resampling Plans.* SIAM, 1982, vol. 38.

[47] M. E. Timmerman, H. A. L. Kiers, and A. K. Smilde, "Estimating confidence intervals for principal component loadings: a comparison between the bootstrap and asymptotic results," *Br. J. Math. Stat. Psychol.*, vol. 60, no. 2, p. 295, 2007.

[48] MathWorks, "Matlab," http://www.mathworks.com/products/matlab.

[49] COMSOL, "Comsol multiphysics modeling software," http://www.comsol.com.

[50] E. D. Palik, *Handbook of Optical Constants of Solids.* Academic Press, 1985.

[51] K. J. Webb and J. Li, "Analysis of transmission through small apertures in conducting films," *Phys. Rev. B*, vol. 73, no. 3, p. 033401, 2006.

[52] ——, "Waveguide cavity surface-enhanced raman scattering," *Phys. Rev. B*, vol. 73, no. 7, p. 073404, 2006.

[53] J. W. Goodman, *Speckle Phenomena in Optics: Theory and Applications.* Roberts and Company Publishers, 2007.

[54] J. C. Maxwell, *A Treatise on Electricity and Magnetism.* Clarendon press, 1881, vol. 1.

[55] E. F. Nichols and G. F. Hull, "The pressure due to radiation," *Phys. Rev.*, vol. 17, pp. 26–50, 1903.

[56] A. Ashkin, J. M. Dziedzic, J. E. Bjorkholm, and S. Chu, "Observation of a single-beam gradient force optical trap for dielectric particles," *Opt. Lett.*, vol. 11, no. 5, pp. 288–290, 1986.

[57] D. J. Wineland and W. M. Itano, "Laser cooling of atoms," *Phys. Rev. A*, vol. 20, no. 4, p. 1521, 1979.

[58] V. B. Braginski and A. B. Manukin, "Ponderomotive effects of electromagnetic radiation," *Sov. Phys. JETP*, vol. 25, no. 4, pp. 653–655, 1967.

[59] A. Dorsel, J. D. McCullen, P. Meystre, E. Vignes, and H. Walther, "Optical bistability and mirror confinement induced by radiation pressure," *Phys. Rev. Lett.*, vol. 51, no. 17, p. 1550, 1983.

[60] T. J. Kippenberg, H. Rokhsari, T. Carmon, A. Scherer, and K. J. Vahala, "Analysis of radiation-pressure induced mechanical oscillation of an optical microcavity," *Phys. Rev. Lett.*, vol. 95, no. 3, p. 033901, 2005.

[61] S. Gigan, H. R. Böhm, M. Paternostro, F. Blaser, G. Langer, J. B. Hertzberg, K. C. Schwab, D. Bäuerle, M. Aspelmeyer, and A. Zeilinger, "Self-cooling of a micromirror by radiation pressure," *Nature*, vol. 444, no. 7115, p. 67, 2006.

[62] A. Abramovici, W. E. Althouse, R. W. Drever, Y. Gürsel, S. Kawamura, F. J. Raab, D. Shoemaker, L. Sievers, R. E. Spero, K. S. Thorne, R. E. Vogt, R. Weiss, S. E. Whitcomb, and M. E. Zucker, "Ligo: The laser interferometer gravitational-wave observatory," *Science*, vol. 256, no. 5055, pp. 325–333, 1992.

[63] B. P. Abbott, R. Abbott, T. D. Abbott, M. R. Abernathy, F. Acernese, K. Ackley, C. Adams, T. Adams, P. Addesso, R. X. Adhikari *et al.*, "Observation of gravitational waves from a binary black hole merger," *Phys. Rev. Lett.*, vol. 116, no. 6, p. 061102, 2016.

[64] O. Arcizet, T. Briant, A. Heidmann, and M. Pinard, "Beating quantum limits in an optomechanical sensor by cavity detuning," *Phys. Rev. A*, vol. 73, no. 3, p. 033819, 2006.

[65] K. J. Webb and Shivanand, "Negative electromagnetic plane-wave force in gain media," *Phys. Rev. E*, vol. 84, no. 5, p. 057602, 2011.

[66] M. Mansuripur, A. R. Zakharian, and E. M. Wright, "Electromagnetic-force distribution inside matter," *Phys. Rev. A*, vol. 88, p. 023826, 2013.

[67] A. Mizrahi and L. Schächter, "Electromagnetic forces on the dielectric layers of the planar optical bragg acceleration structure," *Phys. Rev. E*, vol. 74, no. 3, p. 036504, 2006.

[68] M. I. Antonoyiannakis and J. B. Pendry, "Electromagnetic forces in photonic crystals," *Phys. Rev. B*, vol. 60, no. 4, p. 2363, 1999.

[69] Please refer to Supplemental Material for details.

[70] A. Einstein and J. Laub, "Über die im elektromagnetischen felde auf ruhende körper ausgeübten ponderomotorischen kräfte," *Ann. Phys.*, vol. 331, no. 8, pp. 541–550, 1908.

[71] P. Penfield and H. A. Haus, *Electrodynamics of Moving Media.* MIT Press, Cambridge, MA, 1967.

[72] K. J. Webb and Shivanand, "Electromagnetic field energy in dispersive materials," *J. Opt. Soc. Am. B*, vol. 27, no. 6, pp. 1215–1220, 2010.

[73] M. C. Sanchez, E. Martin, and J. M. Zamarro, "Unified and simplified treatment of techniques for characterising transmission, reflection or absorption resonators," in *Proc. Inst. Elect. Eng., pt. H*, vol. 137, no. 4. IET, 1990, pp. 209–212.

[74] P. J. Petersan and S. M. Anlage, "Measurement of resonant frequency and quality factor of microwave resonators: Comparison of methods," *J. Appl. Phys.*, vol. 84, no. 6, pp. 3392–3402, 1998.

[75] S. Kim, Y. Xuan, V. P. Drachev, L. T. Varghese, L. Fan, M. Qi, and K. J. Webb, "Nanoimprinted plasmonic nanocavity arrays," *Opt. Express*, vol. 21, no. 13, pp. 15 081–15 089, 2013.

[76] J. R. Moffitt, Y. R. Chemla, S. B. Smith, and C. Bustamante, "Recent advances in optical tweezers," *Annu. Rev. Biochem.*, vol. 77, pp. 205–228, 2008.

[77] E. F. Nichols and G. F. Hull, "The pressure due to radiation.(second paper.)," *Phys. Rev. (Series I)*, vol. 17, no. 1, p. 26, 1903.

[78] L. J. Chu, H. A. Haus, and P. Penfield, "The force density in polarizable and magnetizable fluids," *Proc. IEEE*, vol. 54, no. 7, pp. 920–935, July 1966.

[79] J. P. Gordon, "Radiation forces and momenta in dielectric media," *Phys. Rev. A*, vol. 8, no. 1, pp. 14–21, July 1973.

[80] I. Brevik, "Experiments in phenomenological electrodynamics and the electromagnetic energy-momentum tensor," *Phys. Rep.*, vol. 52, pp. 133–201, 1979.

[81] R. Loudon, S. M. Barnett, and C. Baxter, "Radiation pressure and momentum transfer in dielectrics: The photon drag effect," *Phys. Rev. A*, vol. 71, p. 063802, Jun 2005.

[82] R. N. C. Pfeifer, T. A. Nieminen, N. R. Heckenberg, and H. Rubinsztein-Dunlop, "Momentum of an electromagentic wave in dielectric media," *Rev. Mod. Phys.*, vol. 79, pp. 1197–1216, Oct. - Dec. 2007.

[83] R. V. Jones and B. Leslie, "The measurement of optical radiation pressure in dispersive media," *Proc. Royal Soc. A*, vol. 360, no. 1702, pp. 347–363, Apr. 1978.

[84] A. Ashkin and J. M. Dziedzic, "Radiation pressure on a free liquid surface," *Phys. Rev. Lett.*, vol. 30, no. 4, pp. 139–142, Jan. 1973.

[85] A. Hayat, J. B. Mueller, and F. Capasso, "Lateral chirality-sorting optical forces," *Proc. Natl. Acad. Sci.*, vol. 112, no. 43, pp. 13 190–13 194, 2015.

[86] S. Sukhov, V. Kajorndejnukul, R. R. Naraghi, and A. Dogariu, "Dynamic consequences of optical spin–orbit interaction," *Nat. Photonics*, vol. 9, no. 12, pp. 809–812, 2015.

[87] M. I. Petrov, S. V. Sukhov, A. A. Bogdanov, A. S. Shalin, and A. Dogariu, "Surface plasmon polariton assisted optical pulling force," *Laser Photonics Rev.*, vol. 10, no. 1, pp. 116–122, 2016.

[88] S. Wang and C. T. Chan, "Strong optical force acting on a dipolar particle over a multilayer substrate," *Opt. Express*, vol. 24, no. 3, pp. 2235–2241, 2016.

[89] X. Cui, S. Wang, and C. T. Chan, "Superlens induced loss-insensitive optical force," *Opt. Express*, vol. 24, no. 13, pp. 13 992–13 998, 2016.

[90] A. Novitsky, C.-W. Qiu, and H. Wang, "Single gradientless light beam drags particles as tractor beams," *Phys. Rev. Lett.*, vol. 107, no. 20, p. 203601, 2011.

[91] A. Mizrahi and Y. Fainman, "Negative radiation pressure on gain medium structures," *Opt. Lett.*, vol. 35, no. 20, pp. 3405–3407, 2010.

[92] K. J. Webb, "Dependence of the radiation pressure on the background refractive index," *Phys. Rev. Lett.*, vol. 111, no. 4, p. 043602, July 2013.

[93] ——, "Relationship between the einstein-laub electromagnetic force and the lorentz force on free charge," *Phys. Rev. B*, vol. 94, no. 6, p. 064203, 2016.

[94] D. Middleton, *An Introduction to Statistical Communication Theory*. IEEE Press, 1996.

[95] P. B. Johnson and R. W. Christy, "Optical constants of the noble metals," *Phys. Rev. B*, vol. 6, no. 12, p. 4370, 1972.

[96] D. E. Aspnes and A. A. Studna, "Dielectric functions and optical parameters of Si, Ge, GaP, GaAs, GaSb, InP, InAs, and InSb from 1.5 to 6.0 eV," *Phys. Rev. B*, vol. 27, no. 2, p. 985, 1983.

[97] K. Seal, D. A. Genov, A. K. Sarychev, H. Noh, V. M. Shalaev, Z. C. Ying, X. Zhang, and H. Cao, "Coexistence of localized and delocalized surface plasmon modes in percolating metal films," *Phys. Rev. Lett.*, vol. 97, no. 20, p. 206103, 2006.

[98] A. Cazé, R. Pierrat, and R. Carminati, "Spatial coherence in complex photonic and plasmonic systems," *Phys. Rev. Lett.*, vol. 110, no. 6, p. 063903, 2013.

[99] J. Rosenberg, Q. Lin, and O. Painter, "Static and dynamic wavelength routing via the gradient optical force," *Nat. Photonics*, vol. 3, no. 8, pp. 478–483, 2009.

[100] D. Nikolova, S. Rumley, D. Calhoun, Q. Li, R. Hendry, P. Samadi, and K. Bergman, "Scaling silicon photonic switch fabrics for data center interconnection networks," *Opt. Express*, vol. 23, no. 2, pp. 1159–1175, 2015.

[101] R. Sarma, A. G. Yamilov, S. Petrenko, Y. Bromberg, and H. Cao, "Control of energy density inside a disordered medium by coupling to open or closed channels," *Phys. Rev. Lett.*, vol. 117, no. 8, p. 086803, 2016.

[102] H. A. Atwater, A. R. Davoyan, O. Ilic, D. Jariwala, M. C. Sherrott, C. M. Went, W. S. Whitney, and J. Wong, "Materials challenges for the starshot lightsail," *Nat. Mater.*, p. 1, 2018.

[103] R. E. Collin, *Field Theory of Guided Waves*. McGraw-Hill, 1960.

APPENDICES

A. APPENDIX: ANALYTICAL FIELD SOLUTIONS FOR 1D MULTILAYER STRUCTURES

The field solutions in the Fabry-Perot cavities in Figs. 3.1(a) and (b) can be solved analytically. Each cavity is a 1D multilayer structure that can be treated using an established method [103]. A convenient way to do this is to write the impedance transformation between boundaries m and $m + 1$ as

$$Z_m = \eta_m \frac{Z_{m+1} - i\eta_m \tan k_m l_m}{\eta_m - iZ_{m+1} \tan k_m l_m}, \quad \text{with} \quad m = 4, 3, 2, 1, \tag{A.1}$$

where η_m, k_m, and l_m are the characteristic impedance, phase constant, and thickness, respectively, of the mth region, initialized by $Z_4 = \eta_0$, the free space wave impedance on the right side of M_2 in Fig. 3.1(a). The electric field reflection coefficient on the left boundary in Fig. 3.1(a) is $S_{11} = (Z_1 - \eta_0)/(Z_1 + \eta_0)$, where we have used scattering parameter notation. The total electric and magnetic fields at Boundary 1 are thus $E_1 = (1 + S_{11})E_0$ and $H_1 = (1 - S_{11})E_0/\eta_0$, where E_0 is the incident electric field phasor. Then, the electric and magnetic fields everywhere in this 1D multilayer structure can be calculated from

$$\begin{bmatrix} E_{m+1} \\ H_{m+1} \end{bmatrix} = \begin{bmatrix} \cos k_m l_m & i\eta_m \sin k_m l_m \\ i\eta_m^{-1} \sin k_m l_m & \cos k_m l_m \end{bmatrix} \begin{bmatrix} E_m \\ H_m \end{bmatrix}, \quad \text{with} \quad m = 4, 3, 2, 1, \tag{A.2}$$

initialized by E_1, H_1. The field solutions allow the stored energy W, the cavity Q, the force densities in the mirrors and hence the pressure to be obtained. The fields in the asymmetric Fabry-Perot cavity shown in Fig. 3.1(b) can be likewise found.

B. APPENDIX: COMPARISON BETWEEN MAXWELL'S MOMENTUM PICTURE AND FORCE DENSITY DESCRIPTION

In Chap. 3, we calculated the pressure from the utilization of force density described in (3.1). Therefore, the interaction between fields and materials can be captured. On the other hand, many other works use the momentum exchange picture proposed by Maxwell [54] and calculate pressure by the intensity in the cavity under high finesse cavity approximation. Here, we want to compare the pressures based on these two approaches. We choose AFP2 and AFP3 (the nomenclature means the asymmetric cavity in Fig. 3.1(b) and the parameters are given in Table 3.1) which provide stronger pressure enhancement and higher Q in the Fabry-Perot cavity examples in Chap. 3. The results of AFP2 and AFP3 are shown in Fig. B.1 (a) and (b), respectively. In Fig. B.1 (a), the red square signs are from Fig. 3.2 (b) which are calculated from the integral of force density within the scattering material in M_2 using (3.1). The black square signs are estimated from Maxwell's picture where the radiation pressure is $(1 + |\Gamma|^2)S_{m2}/v$ [54], when there is no transmission through the cavity, where Γ is the reflection coefficient on M_2, S_{m2} is the intensity illuminated into M_2, v is the speed of light, equal to c in free space. In Fig. B.1 (b), the blue stars are again calculated from (3.1) and the black stars from Maxwell's picture. We can observe the slight difference between the pressure calculated from two approaches due to the influence within the scattering materials, but generally, Maxwell's picture provides a good estimate on the pressure for the Fabry-Perot cavity examples.
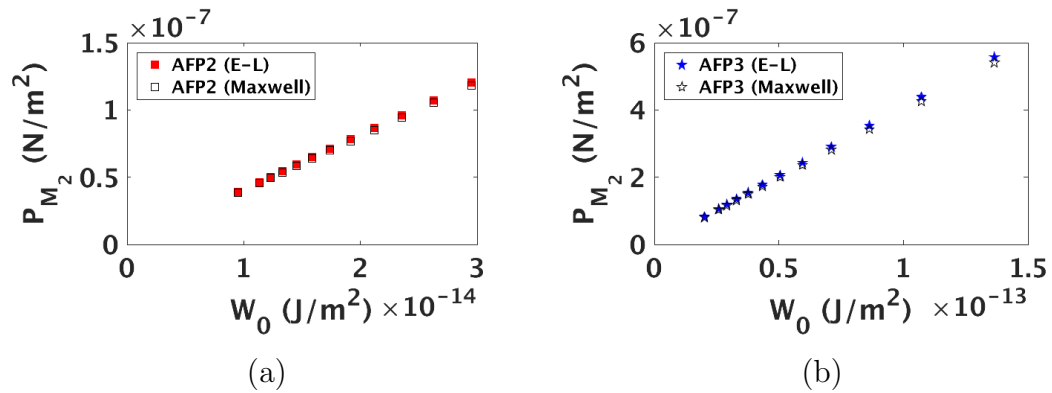
Fig. B.1. (a) Radiation pressure P_{M_2} as a function of stored energy W_0 for asymmetric Fabry-Perot cavity AFP2. The red square signs are from Fig. 3.2 (b) which are calculated from the integral of force density within scattering material using Einstein-Laub description. The black square signs are estimated from Maxwell's momentum picture where the radiation pressure is $(1+|\Gamma|^2)S_{m2}/c$, when there is no transmission through the cavity, where Γ is the reflection coefficient on M_2, S_{m2} is the intensity illuminated on M_2, c is the speed of light. (b) P_{M_2} from Einstein-Laub force density description (blue stars) and from Maxwell's momentum picture (black stars) for AFP3.